

Transient Brittle Creep mechanism explains early postseismic phase of the 2011 Tohoku-Oki megathrust earthquake: observations by high-rates GPS solutions

Axel Periollat¹, Mathilde Radiguet¹, Jérôme Weiss², Cedric Twardzik³, David Amitrano⁴, Nathalie Cotte⁵, Lou Marill¹, and Anne Socquet⁶

¹ISTerre

²French National Centre for Scientific Research (CNRS)

³University of Strasbourg

⁴ISTerre, Université Grenoble Alpes

⁵University Joseph Fourier / CNRS

⁶Université Grenoble Alpes

November 22, 2022

Abstract

The early stage of the postseismic phase is characterized by a large deformation rate. Its analysis is thus key to decipher the role played by different mechanisms (afterslip and viscoelasticity) at various time scales. Here, we process GPS data to obtain 30-seconds kinematic position time series recording the surface deformation following the Mw 9.0 Tohoku-Oki megathrust earthquake (2011), and combine them with static solutions over 9 years. We analyze the temporal evolution of the time series and use these observations to image the postseismic slip. We find that the first month of deformation following Tohoku-Oki can be explained by an afterslip mechanism, that exhibits an “Omori-like” decay, with a p -value around 0.75 almost everywhere with the exception of a small region around Ibaraki prefecture where $p \sim 1$ is observed. This $p < 1$ indicates that the postseismic displacements do not increase logarithmically with time as predicted by rate-and-state rheology. Instead, we argue that early afterslip is associated to a transient brittle creep mechanism. We use numerical simulations to show that an exponent of $p < 1$ can be explained by a combination of thermal activation of local slips and elastic interactions. Over longer time scales, an additional mechanism is required to explain the observed deformation signal, and the transient brittle creep mechanism is combined with viscoelastic relaxation modeled by a Newtonian flow. The spatial analysis reveals two distinct afterslip regions, a major one on the North, associated with a p -value around 0.75, and a smaller one close to the Ibaraki aftershock, associated to $p \sim 1$.

Hosted file

supporting_information_periollat_2022_jgr_solid_earth.docx available at <https://authorea.com/users/536249/articles/599001-transient-brittle-creep-mechanism-explains-early-postseismic-phase-of-the-2011-tohoku-oki-megathrust-earthquake-observations-by-high-rates-gps-solutions>

1
2 **Transient Brittle Creep mechanism explains early postseismic phase of the 2011**
3 **Tohoku-Oki megathrust earthquake: observations by high-rates GPS solutions**
4

5 **Axel Periollat^{*1}, Mathilde Radiguet¹, Jérôme Weiss¹, Cédric Twardzik², David Amitrano¹,**
6 **Nathalie Cotte¹, Lou Marill¹, and Anne Socquet¹**

7 ¹Univ. Grenoble Alpes, Univ. Savoie Mont Blanc, CNRS, IRD, Univ. Gustave Eiffel, ISTerre,
8 38000 Grenoble, France

9 ²Institut de Physique du Globe de Strasbourg, UMR 7516, Université de Strasbourg, EOST,
10 CNRS, Strasbourg, France

11
12 Corresponding author: Axel Periollat (axel.periollat@univ-grenoble-alpes.fr)

13 **Key Points:**

- 14 • Kinematic and static positions time series are used to analyse the postseismic deformation
15 following the M_w 9.0 Tohoku-Oki earthquake
- 16 • The temporal evolution of the early postseismic is explained by an Omori-like Transient
17 Brittle Creep mechanism with a p -value around 0.75
- 18 • The spatial analysis reveals a major afterslip zone downdip from the main rupture and a
19 secondary one close to the Ibaraki-Oki event

20 Abstract

21

22 The early stage of the postseismic phase is characterized by a large deformation rate. Its analysis
23 is thus key to decipher the role played by different mechanisms (afterslip and viscoelasticity) at
24 various time scales. Here, we process GPS data to obtain 30-seconds kinematic position time
25 series recording the surface deformation following the Mw 9.0 Tohoku-Oki megathrust
26 earthquake (2011), and combine them with static solutions over 9 years. We analyze the
27 temporal evolution of the time series and use these observations to image the postseismic slip.
28 We find that the first month of deformation following Tohoku-Oki can be explained by an
29 afterslip mechanism, that exhibits an “Omori-like” decay, with a p -value around 0.75 almost
30 everywhere with the exception of a small region around Ibaraki prefecture where $p \sim 1$ is
31 observed. This $p < 1$ indicates that the postseismic displacements do not increase logarithmically
32 with time as predicted by rate-and-state rheology. Instead, we argue that early afterslip is
33 associated to a transient brittle creep mechanism. We use numerical simulations to show that an
34 exponent of $p < 1$ can be explained by a combination of thermal activation of local slips and
35 elastic interactions. Over longer time scales, an additional mechanism is required to explain the
36 observed deformation signal, and the transient brittle creep mechanism is combined with
37 viscoelastic relaxation modeled by a Newtonian flow. The spatial analysis reveals two distinct
38 afterslip regions, a major one on the North, associated with a p -value around 0.75, and a smaller
39 one close to the Ibaraki aftershock, associated to $p \sim 1$.

40

41 Plain Language Summary

42

43 The Tohoku-Oki earthquake of March 11, 2011, is one of the largest subduction earthquake of
44 the past decade. Earthquakes produce a perturbation in the state of the stress of the crust and
45 mantle, and this perturbation is relaxed after the earthquake, during the postseismic phase. This
46 phase is associated with deformations measurable at the earth surface with instruments such as
47 GPS stations. These measurements can be used to infer the different processes involved in this
48 relaxation, among which the one called afterslip, which corresponds to the aseismic slip that
49 occur at depth around the fault zone. The originality of our study is the inclusion of the GPS
50 signal from the first few minutes, to constrain the details of the early postseismic deformation.
51 We find that the early postseismic phase could be described by a different modeling than the one
52 commonly used by the community with an evolution as a logarithm of time. We have identified a
53 major region downdip of the Tohoku-Oki rupture zone and another small area near the large
54 aftershock is identified with different temporal evolution. Further studies on large earthquakes
55 should consider these results to revisit and review the early postseismic phase after large
56 subduction earthquakes.

57

58 **1 Introduction**

59

60 Following large earthquakes, the state of stress of the surrounding earth crust and mantle is
61 modified, triggering aftershocks and various aseismic processes, in the so called postseismic
62 phase. Aftershocks represent a small portion of the energy released in this postseismic phase, and
63 aseismic processes, among which afterslip (transient frictional sliding on the fault), mantellic
64 viscoelastic relaxation in the mantle, and/or poroelastic rebound are considered to dominate.
65 These mechanisms involve different spatial and temporal scales, and it is not trivial to
66 differentiate between them based on the deformation signal observed at the surface (Ingleby &
67 Wright, 2017).

68

69 A detailed analysis of the temporal evolution of the deformation is necessary to identify the
70 underlying mechanisms at play at both short (minutes to days) and long (years) timescales. The
71 early stages of the postseismic phase, from a few minutes to a few hours after the mainshock, are
72 characterized by high deformation rates. Analyzing the deformation in this early period can bring
73 strong constraints on the postseismic behavior. Yet, the early postseismic deformation has been
74 little studied, because high-rate time series of the surface deformation in the vicinity of the
75 rupture zone are not easily available and, when available, it is complex to detect signal at this
76 early stage due to the larger noise level of the high-rate time series compared to traditional daily
77 position time series (Twardzik et al., 2019).

78

79 The recent devastating megathrusts earthquakes (Sumatra, Chile and Japan) significantly
80 increased our understanding of the postseismic phase. In particular, the M_w 9.0 Tohoku
81 earthquake was recorded with unprecedented high resolution in space and time, and provides a
82 unique opportunity to analyze the postseismic relaxation, including in its early stage. For these
83 large subduction earthquakes, afterslip and viscoelastic relaxation have been identified as the
84 most important mechanisms (*e.g.* Wang et al., 2012) to explain the observed deformation.
85 Instead, the contribution of the poroelastic rebound to the inland displacement was shown to be
86 small for the Tohoku-Oki event (Hu et al., 2014).

87

88 Deciphering the contributions of afterslip and viscoelastic relaxation in the postseismic
89 deformation signal, notably in the early stages remains a difficult problem. Postseismic models
90 assuming an elastic earth (Ozawa et al., 2012) tend to substantially overestimate the amount of
91 afterslip compared to viscoelastic models including a transient viscosity (Sun et al., 2014; Sun &
92 Wang, 2015). Several studies considered that afterslip is the dominant mechanism at short time
93 scales (Hsu, 2006; Perfettini et al., 2010; Perfettini & Avouac, 2014), and it is generally modeled
94 using the rate-and-state formalism, with afterslip occurring in a region with a velocity-
95 strengthening friction regime. Within a steady-state approximation of the rate-and-state law
96 (Dieterich, 1979; Marone et al., 1991), a logarithmic increase of slip with time is predicted from
97 the rate-and-state formulation. This temporal evolution matches the aftershock decay rates,
98 leading to the hypothesis that aftershocks are driven by afterslip (Perfettini & Avouac, 2004).
99 However, the importance of viscoelastic relaxation in the first year of the deformation has been
100 evidenced for the Tohoku-Oki earthquake by the landward motion recorded by offshore geodetic
101 data, motion that can only be explained by viscoelastic deformation (Sun et al., 2014; Sun &
102 Wang, 2015), and modeled using low transient viscosities in the mantle.

103

104 Previous studies investigating the early postseismic phase of large earthquakes are still quite rare,
105 and include the M_w 6.4 2004 Parkfield earthquake (Langbein, 2006), the M_w 8.1 2003 Tokachi-
106 Oki earthquake (Fukuda et al., 2009, 2013; Miyazaki & Larson, 2008), the M_w 7.2 2012 Nicoya
107 earthquake (Malservisi et al., 2015), and more recently the M_w 7.8 2016 Pedernales earthquake
108 (Tsang et al., 2019), the M_w 8.3 Illapel earthquake (Twardzik et al., 2021) and a compilation of
109 studies including 4 megathrusts in South America (Twardzik et al., 2019). All these studies
110 reveal the importance of early postseismic deformation, and the fact that measurements made
111 using daily GNSS solutions can lead to a significant overestimation of the coseismic offsets.
112 Concerning the mechanisms involved at this early stage, Langbein (2006) and Morikami &
113 Mitsui (2020) show that the GPS data starting from a few minutes after the mainshock are
114 adequately fitted by an « Omori-like » evolution of the velocity, *i.e.* $v \sim 1 / t^p$ and $p < 1$. Fukuda
115 et al. (2009) suggested that the Tokachi-Oki relaxation follows the prediction from the full rate-
116 and-state formulation, including the acceleration phase (Perfettini & Ampuero, 2008). However,
117 an alternative explanation for this apparent acceleration is the perturbation due to an early
118 aftershock (Miyazaki & Larson, 2008).

119

120 We take advantage of the dense inland GPS network in Japan to investigate the postseismic
121 deformation mechanisms after the great Tohoku-Oki earthquake which occurred on March 11,
122 2011 at 05:46:24 (UTC) near the northeast coast of Honshu. This earthquake has been widely
123 recorded with various datasets, such as inland seismic and/or geodetic data, seafloor geodetic
124 observations and tsunami data. Previous studies of the co-seismic phase feature a ~400 km
125 (along strike) by ~150 km along dip slipping area, with a maximum slip that sometimes exceeds
126 50 meters at shallow depth close to the trench (see for a review Lay, 2018; Tajima et al., 2013;
127 Wang et al., 2018). Previous works have been done on the postseismic phase of the Tohoku-Oki
128 earthquake. Some only considered afterslip (Ozawa et al., 2012; Perfettini & Avouac, 2014) and
129 revealed a large afterslip patch downdip from the co-seismic slip and possibly shallow afterslip
130 (Perfettini & Avouac, 2014). Others also take into account the contribution from viscoelastic
131 deformation (*i.e.* Sun et al., 2014; Sun & Wang, 2015). Two studies analyzed the early post-
132 seismic phase of the Tohoku-Oki earthquake Munekane (2012), and Morikami & Mitsui (2020)
133 using high-rate kinematic GPS data, revealing some details about the kinematics of the post-
134 seismic phase, but without providing details on the possible mechanisms. In this study, we want
135 to explore further the post-seismic phase of the Tohoku-Oki earthquake, more specifically at its
136 early stages, and provide a mechanical interpretation about the observed evolution of
137 deformation.

138

139 In this study, we characterize the temporal evolution of the postseismic deformation from
140 minutes to years after the Tohoku-Oki event, combining 30-seconds kinematic GPS data for the
141 early stages (from 10 minutes to 1 month) after the coseismic rupture and daily solutions for
142 longer time scales (from 1 month to ~9 years). Then, we use simple analytical models to explain
143 the temporal evolution of our data with the goal to constrain the mechanisms and the rheology of
144 this postseismic phase. Following Montési (2004), we associate each temporal evolution to a
145 given rheological model (afterslip, viscoelastic relaxation). Despite its simplicity, our approach
146 aims at discussing the mechanisms at stake, and thus goes further than curve fitting approaches
147 (Sobrero et al., 2020; Tobita, 2016) which only focus on finding the set of function minimizing
148 the residuals.

149
 150 Section 2 describes the GPS data used, processing methods employed to obtain the position time
 151 series, and the post-processing. In Section 3, we model the observed postseismic surface
 152 displacement using different rheological models. We show that afterslip with an “Omori-like”
 153 evolution of the velocity and an exponent of $p < 1$ best fits our early postseismic data. We check
 154 how the model explains the observation at larger time-scales (~9 years) and we show that we
 155 should combine afterslip and viscoelastic relaxation. We discuss the physical meaning of the
 156 exponential decay and its implications for the fault rheology. In Section 4, we focus on the
 157 spatial pattern of postseismic slip by inverting the observed surface displacements to locate slip
 158 on the plate interface. We produce coseismic slip models for the mainshock and the largest M_w
 159 7.7 Ibaraki-Oki aftershock which occurred ~30 minutes after the mainshock. Then, different time
 160 windows of increasing length are used to investigate the spatio-temporal evolution of the
 161 postseismic slip. Both analysis in Section 3 and 4 allow us to determine two separate types of
 162 behaviors. The first concerns regions which are directly affected by the Tohoku-Oki event, the
 163 other is a small region near the Ibaraki-Oki rupture area. In Section 5, we discuss the observed
 164 results, in particular the significance of the exponent $p < 1$ found in our temporal evolution, in the
 165 light of results coming from numerical mechanic modelling.

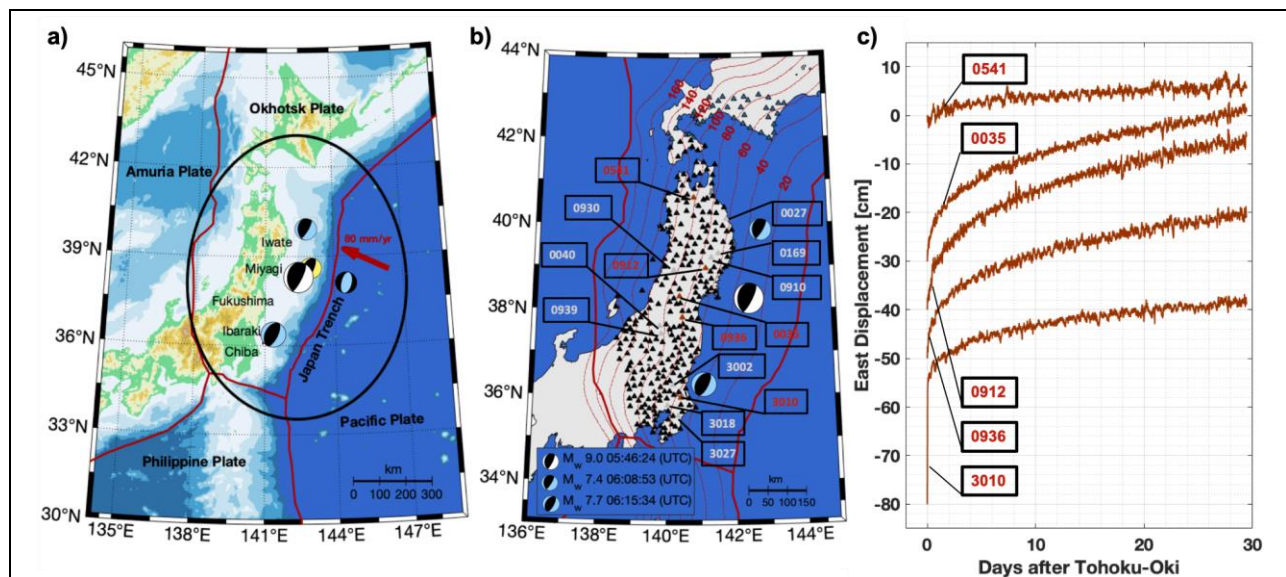
166

167 2 GPS Data Analysis

168

169 The *GPS Earth Observation Network* (GEONET) network in Japan consists in around 1200
 170 permanent GPS stations. In this study, we selected the 318 stations within a distance of 500 km
 171 from the Tohoku-Oki epicenter, which correspond to the stations that recorded the Tohoku-Oki
 172 mainshock, its main aftershocks (Figure 1a-b) and the postseismic signal (Nishimura et al.,
 173 2011).

174



175

176

177 **Figure 1 | Maps of the Japan Area and examples of GPS kinematic time series. a.** Plate
 178 boundaries are illustrated in red, the associated Pacific interseismic loading (~80 mm/yr) is

179

179 represented with the red arrow. Significant earthquake focal mechanisms (F-net catalogue) sorted
 180 by size (yellow as foreshock, black as mainshock, black and blue as largest aftershocks). Stations
 181 used for this study are located within the black circle (distance from the mainshock epicenter less
 182 than 500 km). **b.** Black triangles are stations used for this study, brown triangles illustrate
 183 stations shown on Figure 1c, grey triangles are stations represented on Figures 2, 3, 5 and 6 and
 184 blue triangles are stations used to build the stack for the common modes correction. Earthquakes
 185 recorded by our kinematic data are the mainshock as well as the Ibaraki-Oki and largest north
 186 aftershock. Plates boundaries (red lines) and isodepth of the fault are given (red thinny lines). **c.**
 187 Postseismic signal from five different stations (shown on Figure 1b) on East component after the
 188 kinematic processing and post-processing phases applied (Sidereal Filtering and Removing
 189 Common Modes).

190
 191 Our study is a compilation of two distinct GPS processing strategy: i) the first month after the
 192 mainshock is processed with high-rate kinematic 30-seconds solutions to investigate in details
 193 the fast motion at the beginning of the postseismic phase, and ii) from one month to ~9 years
 194 after the mainshock the time series are extended with daily solutions from static processing. In
 195 each case, the time series are processed with the Precise Point Positioning (PPP) approach
 196 (Zumberge et al., 1997), using the GIPSYX-1.3 software developed by the Jet Propulsion
 197 Laboratory (JPL). This single receiver approach requires high accuracy on satellites clocks and
 198 orbits (Bertiger et al., 2010). We used the final JPL clock corrections and orbits
 199 <http://www.igs.org/products> defined in the IGS14 reference frame (Altamimi et al., 2016).
 200 Tropospheric delays and gradients are estimated (every 30-secondes) using VMF1 mapping
 201 functions (Boehm et al., 2006) and we consider high order ionospheric terms using the IRI-2012
 202 model (Bilitza et al., 2014). Ocean-loading effects are corrected using the FES2014b model
 203 (Spiridonov & Vinogradova, 2020). An elevation mask of 7 degrees is used. Antenna and
 204 radome models are used to correct phase center variations on antennas.

205
 206 For the high rate positions, our processing strategy is similar to the multi-step iterative method
 207 described by Twardzik et al., (2019). To reduce high frequency noise in the time series, a
 208 Kalman filter is used during the processing of the GPS data, and the associated randomwalk
 209 parameters are selected to be suitable for detecting slow processes over time scales of hours to
 210 days. Following (Twardzik et al., 2019), and consistently with Choi (2007), we used $9.0e-5$ m/ \sqrt{s}
 211 for the troposphere zenith random walk parameter and $3.0e-4$ m/ \sqrt{s} for the random walk
 212 parameter of the Kalman filter for the kinematic positioning. We process separately the data
 213 from one month before the earthquake up to the origin time of the earthquake, and from 10
 214 minutes after the origin time ($t_0^* = t_0 + 10$ minutes) to one month after the earthquake. We start
 215 the time series at t_0^* to avoid perturbation due to the passing of the seismic waves. This separated
 216 processing for the data before and after the earthquake prevents our estimation of the co-seismic
 217 offset to be biased by the temporal smoothing induced by the kinematic processing. The obtained
 218 kinematic position times series are still biased by multipath effects due to the reflected waves
 219 recorded by receivers and common modes due to mismodelling of satellites orbits. To correct
 220 multipath effects (see Figure S1a), we build a sidereal filter following Twardzik et al. (2019),
 221 using the signal data from 7 days in the period before the earthquake. We also correct the time
 222 series from common modes following the approach of Marquez-Azua & DeMets (2003), by
 223 stacking signals (see Figure S1b) on stations far from coseismic and postseismic effects (blue
 224 triangles locations on Figure 1b).

225

226 We estimate the mean position uncertainty for each individual station and component by
227 calculating the RMS over a period spanning one month before the foreshock (09/02/2011-
228 09/03/2011). To quantify the improvement in time series quality associated with our post-
229 processing, we estimated the RMS on each component, and we average over all stations. Our
230 corrections lead to a global RMS reduction from 9.1 to 6.3 mm and from 9.5 to 7.0 mm on the
231 North and East components respectively. The RMS reduction on the Vertical component is low
232 (from 22 to 21 mm); this is expected as the Vertical component is highly sensitive to local
233 uncertainties especially in the evaluation of the wet tropospheric delay. This, combined with a
234 low postseismic signal on this component, implies poor signal to noise ratio on the Vertical.
235 Consequently, we did not include vertical time series in the temporal subsequent analysis.

236

237 To summarize, our dataset consists of 30-s kinematic time series starting from 10 minutes after
238 the earthquake origin time (t_0^* : 05:56:00 UTC) and up to 1 month after Tohoku-Oki, which we
239 complete with daily solutions up to ~ 9 years after the mainshock. Among the 318 stations
240 processed, five examples of final kinematic position time series are shown on Figure 1.c, with
241 their locations indicated as brown triangles on Figure 1.b. For all the data (kinematic and daily
242 static processing), we detrend the time series by removing the interseismic velocity, in order to
243 focus on the postseismic signal only. The interseismic trend was estimated using a trajectory
244 model (Marill et al., 2021), over a two years period (2009-2011) prior the earthquake (see Figure
245 S2). Even if we start 10 minutes after the earthquake origin time, we were able to capture the co-
246 seismic displacements of two large aftershocks. The first aftershock is a M_w 7.4 (06:08:53 UTC)
247 located north of the mainshock, and we find some sites along the Miyagi-Iwate coast showing a
248 coseismic displacement of a few centimeters. The second is the M_w 7.7 Ibaraki-Oki (06:15:34
249 UTC) earthquake, south of the mainshock (Figure 1a-b). Stations near the largest aftershock
250 location, as station 3010 on the Figure 1c, show a well detected coseismic offset, partially
251 smoothed by the Kalman Filter during the GNSS processing. We estimate the offsets due to the
252 aftershocks using a time window from 9 to 27 minutes after t_0^* which allows to account for the
253 smoothed offsets. This estimated coseismic offset is then removed from the postseismic time
254 series which we analyze.

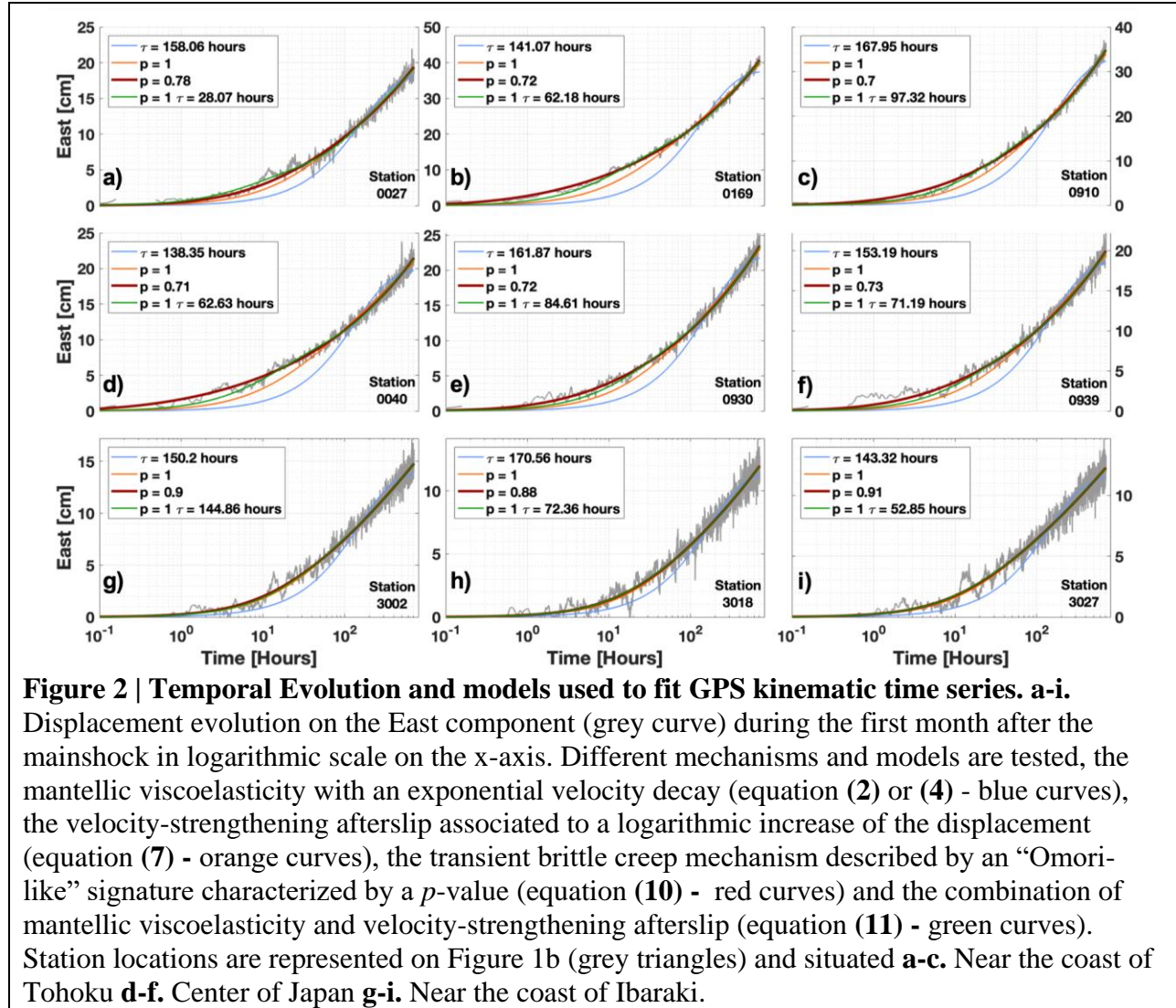
255

256 **3 Modelling Postseismic Temporal Evolution**

257

258 To model the postseismic temporal evolution, we firstly explore the characteristics of the
259 temporal evolution of the surface displacements during the early stage of the postseismic phase,
260 defined as the first month following the Tohoku-Oki earthquake. Then, using our daily solutions,
261 we extended this analysis to a longer timescale of ~ 9 years.

262



263
264
265
266
267
268
269
270
271
272
273
274

275 3.1 Early Postseismic Deformation

276

277 In what follows, we consider that the stresses resulting from the coseismic rupture induce a
278 postseismic relaxation accommodated by viscoelasticity in the mantle, afterslip, or a combination
279 of both. Coupling this with an elastic crust from a simple conceptual model (Rice & Tse, 1986)
280 gives rise to different expressions for the time evolution of surface velocities and displacements.
281 These expressions are then compared to our GPS time series to discuss the underlying
282 mechanisms at play. Using non-linear least-squares inversion, we compute parameters and
283 uncertainties of the different models on surface displacement time series. We invert parameters
284 for the East and North component to adjust postseismic kinematic position time series. Results
285 obtained on East and North components are consistent but we choose to represent only results
286 obtained on the East component which has the largest deformation amplitude, due to the
287 mainshock location and the thrust faulting mechanism. Figure 2 shows the East component from

288 surface displacements of GPS stations located near Tohoku (Figure 2.a-c), in the central Honshu
 289 (Figure 2.d-f) and close to the Ibaraki coast (Figure 2.g-i). The location of these stations is given
 290 on Figure 1.b (grey triangles). The data gap between 9 and 27 minutes after t_0^* results from the
 291 removal of the period because of the occurrence of the two largest aftershocks recorded.

292 Hereafter, the different possible mechanisms of postseismic deformation and the associated
 293 models are described, with the related data fitting description (see Figure 2).
 294

295 3.1.1 Viscoelastic Relaxation

296

297 The first possible mechanism for postseismic deformation is related to the viscoelasticity of the
 298 mantle, which is commonly modeled from a Burgers rheology represented by a combination of a
 299 Maxwell fluid of viscosity η_M and shear modulus G_M , and a Kelvin solid of viscosity η_K and
 300 shear modulus G_K (Sun et al., 2014; Sun & Wang, 2015; Wang et al., 2012). The Kelvin,

301 $\tau_K = \frac{\eta_K}{G_K}$ and Maxwell $\tau_M = \frac{\eta_M}{G_M}$ characteristic timescales are usually defined with $\tau_K \ll \tau_M$.

302 Consequently, the transient Kelvin component of the rheology is considered to be predominant at
 303 short timescales, while the Maxwell component dominates at long timescales. Thus, in an early
 304 postseismic regime, a viscoelastic mantle submitted to a constant stress σ should give rise to a
 305 velocity $v(t)$ of the form:

$$306 \quad v(t) = v_0 e^{-\frac{t}{\tau_K}} \quad (1),$$

307 with the initial postseismic velocity $v_0 = v(t = 0)$. Consequently the surface displacement $u(t)$
 308 is given by the relation:

$$309 \quad u(t) = v_0 \tau_K (1 - e^{-\frac{t}{\tau_K}}) \quad (2).$$

310 A best-fitting attempt of our GPS kinematic time series with expression (2), with τ_K and the
 311 prefactor v_0 as adjustable parameters, clearly fails to reproduce the observations (blue curves on
 312 Figure 2). At longer timescales, the Maxwell component would add, under a constant stress, a
 313 constant velocity term proportional to η_M , *i.e.* a displacement increasing linearly with time,
 314 which is not observed in our data. However, in this case, a Newtonian flow of the mantle would
 315 relax the stress induced by the coseismic rupture, leading to a feedback loop between a
 316 decreasing stress and a stress-dependent rheology. To take this into account, following many
 317 others (Helmstetter & Shaw, 2009; Marone et al., 1991; Montési, 2004), we can write:

$$318 \quad \frac{d\sigma}{dt} = -k(v_i - v(t)) \quad (3),$$

319 where v_i is the interseismic velocity resulting from tectonic loading and k a stiffness parameter
 320 representing the elastic stiffness of the lithosphere. This interseismic velocity (\sim cm/year) is
 321 negligible compared to our recorded early postseismic velocities (\sim cm/hour to cm/day). In
 322 addition, the time series have been corrected from the interseismic trend (see Figure S2). As
 323 (Montési, 2004) mentioned, coupling expression (3) with a Newtonian creep (*i.e.* $v \sim \sigma$) within a
 324 layer of thickness H predicts an exponential decay of the velocity that mimics equation (1),
 325 hence leading to an expression similar to (2) for the displacement as,

$$326 \quad u(t) = v_0 \tau_* (1 - e^{-\frac{t}{\tau_*}}) \quad (4),$$

327 with a characteristic timescale $\tau_* = kH\eta_M$ (Montési, 2004). Note that although expressions (2)
 328 and (4) are similar, they correspond to different physical mechanisms.

329 As detailed below, early (~month) Tohoku-Oki postseismic deformation is characterized by an
 330 absence of a common characteristic timescale, in qualitative agreement with previous
 331 observations for other earthquakes (Savage et al., 2005). This rules out a predominant role of
 332 viscoelastic relaxation of the mantle during the early stage of the postseismic phase. We will
 333 discuss in more details below its possible role at longer timescales (~years).

334

335 3.1.2 Velocity-Strengthening Afterslip

336

337 We now consider that the elastic stresses induced by the coseismic rupture are relaxed through
 338 afterslip along a “creeping” section of the fault. Following many others (Marone et al., 1991;
 339 Perfettini & Ampuero, 2008), we first assume a velocity-strengthening rate-and-state rheology
 340 for this creeping region. Assuming further a rapid evolution of the state variable, the steady-state
 341 regime of this rheology is given by:

$$342 \quad v = v_* e^{\frac{\sigma - \sigma_*}{a - b}} \quad (5),$$

343 where σ_* is the stress supported by the fault for a reference velocity v_* while a and b are the
 344 classical rate-and-state parameters. Coupling this rheology with relation (3) and a negligible
 345 interseismic loading rate ($v_i \ll v$) leads to a velocity history of the form (Montési, 2004), (see
 346 the conceptual model on Figure S3):

$$347 \quad v(t) = v_0 \frac{c}{t + c} \quad (6),$$

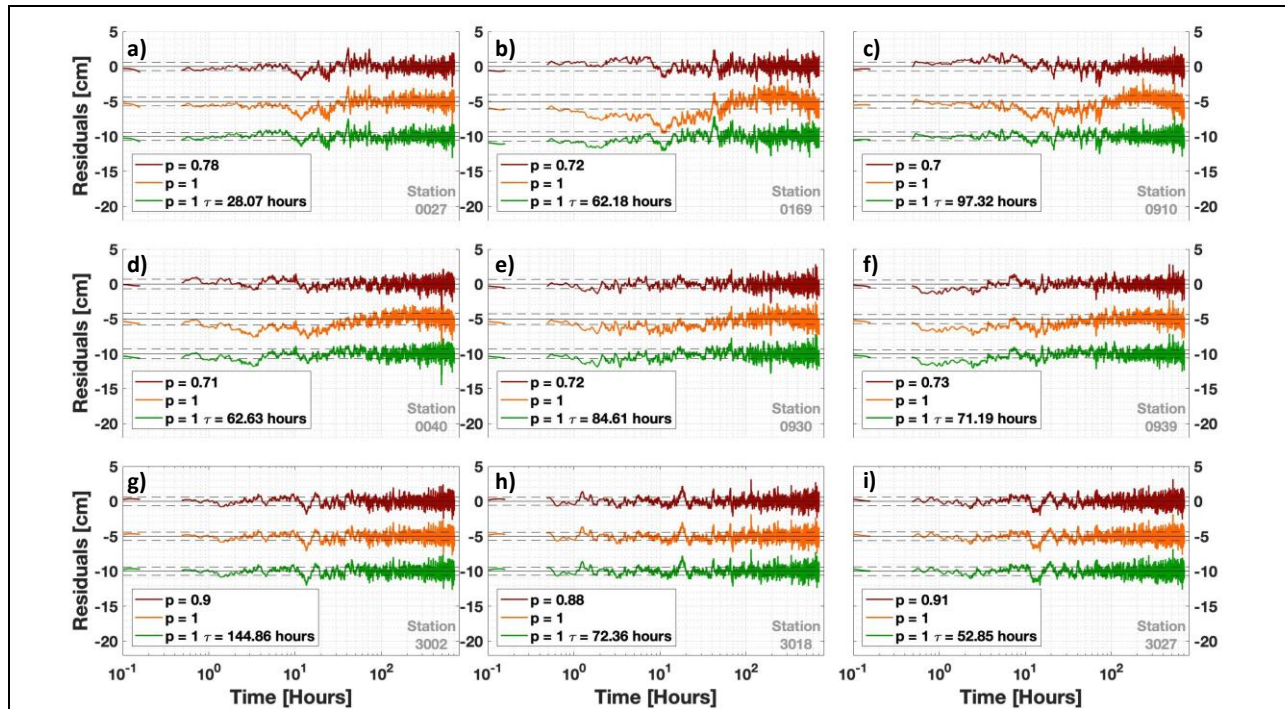
348 with c a time constant depending on the rate-and-state parameters and the stiffness k . This then
 349 leads to a logarithmic increase of the displacement:

$$350 \quad u(t) = cv_0 \ln \left(1 + \frac{t}{c} \right) \quad (7).$$

351 Note that, in these expressions, c does not represent a characteristic *time-decay* for the velocity
 352 (as τ_K in (1)), but a small *time-delay* before it transitions towards a power law decrease of v while
 353 avoiding a singularity at $t \rightarrow 0$. Expression (7), with c and v_0 as adjustable parameters, fits our
 354 GPS kinematic time series much better than expression (2) (orange curves on Figure 2). Still, it is
 355 shown on Figure 3 that the corresponding residuals are significantly larger than the RMS of the
 356 signal for a majority of the analyzed GPS stations, especially for the first ~forty hours of the
 357 signal. This suggests that a velocity-strengthening rate-and-state rheology at steady-state
 358 improperly models our observations. Nevertheless, we find a small region close to the Ibaraki-
 359 Oki aftershock location where the velocity-strengthening afterslip model seems to properly
 360 explain the surface displacement evolution (Figure 2-3.g-i).

361 The model fails to fit the very early stage (*i.e.*, the first ~40 hours); this could be explained by the
 362 fact that, at short timescales, the steady-state approximation of the rate-and-state formulation is
 363 incorrect (Helmstetter & Shaw, 2009). Releasing this approximation, Perfettini & Ampuero
 364 (2008) performed a numerical analysis of the dynamics of a velocity-strengthening fault patch
 365 following a stress perturbation, and revealed a brief transient acceleration that we do not detect in
 366 our data, followed by a very fast velocity decrease before reaching a $1/t$ decay reminiscent of
 367 expression (6). This is also not compatible with our kinematic GPS observations that show
 368 instead a velocity decay slower than $1/t$ from the onset of postseismic deformation (see below).

369



370
371

372 **Figure 3 | Residuals Analysis. a-i.** Residual displacements on the East component during the
 373 first month after the mainshock in logarithmic scale on the x-axis:
 374 The transient brittle creep mechanism described by an “Omori-like” signature characterized by a
 375 p -value < 1 (equation (10) - red curves), the velocity-strengthening afterslip associated to a $1/t$
 376 decay of the velocity (equation (7) - orange curves) and the combination of mantellic
 377 viscoelasticity and velocity-strengthening afterslip (equation (11) - green curves). Station
 378 locations are represented on Figure 1b (grey triangles) and situated **a-c.** Near the coast of Tohoku
 379 **d-f.** Center of Japan **g-i.** Near the coast of Ibaraki.

380

381 3.1.3 Transient Brittle Creep

382

383 To explain the temporal evolution of postseismic surface displacements, some authors have
 384 invoked a transient creep mechanism within an unruptured section of the fault and its
 385 surroundings (Savage et al., 2005; Savage, 2007). Under constant stress, most of the materials
 386 exhibit initially a transient (primary) creep regime characterized by a decreasing strain-rate,
 387 before reaching a secondary creep regime of constant strain-rate. It has been observed
 388 empirically for a long time, including for rocks (Griggs, 1939) that this primary creep can be
 389 associated, depending on the material and the loading conditions, to a logarithmic increase of the
 390 strain, corresponding to a $1/t$ decay for the strain-rate. In our case, this would translate into
 391 expressions similar to equations (6) and (7) for surface velocities and displacements. Note
 392 however that the physical interpretation of such transient creep within a gouge and/or a damaged
 393 material surrounding the fault is different from a rate-and-state interfacial rheology discussed in
 394 the previous section. Scholz (1968), inspired by previous works on metals (Cottrell, 1952),
 395 proposed to explain this so-called transient logarithmic creep of rocks from the cumulative effect
 396 of numerous stress- and thermally-activated fracturing and local faulting events. We will come
 397 back later to the underlying hypotheses of Scholz’s modelling. Here we just note that this

398 mechanism seems inconsistent with our early postseismic data, as we already stressed that
 399 equation (7) doesn't adequately fit our GPS kinematic position time series. However, such
 400 logarithmic creep appears as a special case rather than a common rule. Indeed, a more generic
 401 empirical expression of transient creep strain-rate $\dot{\epsilon}$, including for rocks (Carter & Kirby, 1978)
 402 is:

$$403 \quad \dot{\epsilon} = A\sigma^n \left(\frac{c}{t+c}\right)^{-p} \exp\left(\frac{-E}{k_B T}\right) \quad (8).$$

404 Where $p \leq 1$, n generally lies in the range $2 \leq n \leq 4$ for rocks, A is a material constant, and the
 405 exponential term accounts for thermal activation characterized by E the activation energy (J), k_B
 406 the Boltzmann constant (J.K⁻¹) and T the temperature (K). In this framework, logarithmic creep
 407 corresponds to the end member where $p = 1$. Historically, Andrade (1910) was the first to report
 408 such power law decay of the strain-rate with p -values lower than 1 for metal wires with $p \approx 2/3$,
 409 which was later called Andrade's creep law. Translating this in terms of postseismic velocities,

$$410 \quad v(t) = v_0(\sigma) \left(\frac{c}{t+c}\right)^{-p} \quad (9a),$$

411 with the stress dependence expressed as,

$$412 \quad v_0(\sigma) = A\sigma^n \quad (9b).$$

413 It leads to the following expression for the displacement:

$$414 \quad u(t) = \frac{v_0 c}{1-p} \left[\left(1 + \frac{t}{c}\right)^{1-p} - 1 \right] \quad (10).$$

415 We fit our GPS kinematic time series with this last expression, with c , p and v_0 as adjustable
 416 parameters, and find on Figure 2 an excellent agreement with our data (red curves) for the first
 417 ~forty hours of the deformation signal. The corresponding residuals shown on Figure 3 (red
 418 curves) are almost flat and remain within the confidence interval determined by the signal RMS.
 419 We create a catalog of parameters and uncertainties obtained from the non-linear least square
 420 inversion. We use the parameter uncertainties to remove from the catalog stations with a poor
 421 signal to noise ratio (those far from the Tohoku-Oki earthquake) or stations with too many data
 422 missing, leaving 203 stations with a reliable estimate of p . Figure 4a shows the spatial pattern of
 423 the p exponent with its statistical distribution on Figure 4b. These figures indicate that most of p
 424 exponents are centered around 0.75. An exception is a small region close to the location of the
 425 Ibaraki-Oki aftershock location where p -values closer to 1 are observed. This observation is
 426 consistent with that made by Morikami & Mitsui (2020) who fitted velocities instead of
 427 displacements with expression (9a). Our results, obtained directly from the fit of the
 428 displacement time series, are more robust as they do not depend on the time-binning chosen to
 429 estimate velocities. The vast majority of the delay times c are of the order of a few hours,
 430 without a clear spatial pattern (see on Figure 4c-d). Figure 4e indicates that the initial velocity v_0
 431 is higher on the Tohoku coast (~4-5 cm/hr), and lower far from mainshock influence (~<1
 432 cm/hr), consistently with a reduced influence of the coseismic stress perturbation. Stations along
 433 the Ibaraki coast are also associated to relatively large initial velocities (~<3cm/hr). Interestingly,
 434 p -values obtained for most of the stations are relatively close to the classical Andrade's exponent
 435 $p=2/3$. Overall, these results suggest that early postseismic deformation following the Tohoku-
 436 Oki earthquake could be explained by "afterslip" associated to a transient brittle creep
 437 mechanism within the gouge and the surrounding material. We will discuss in more details
 438 below the physical interpretation of this transient creep, in particular the signification of the p -
 439 value exponent.

440 In what precedes, we only considered a transient creep rheology under constant stress, *i.e.*
 441 without considering the stress relaxation induced by the deformation. If we now account for
 442 stress relaxation, by coupling this creep rheology (equations (9a) and (9b)) with expression (3), it

443 can be shown that the resulting velocity history is unchanged at small timescales ($t \rightarrow 0$) whatever
 444 the p -value (expression **(9a)**), while at large time scales ($t \rightarrow \infty$), an apparent $1/t$ decay (*i.e.*, $p=1$)
 445 is obtained. In particular, the logarithmic creep behavior (corresponding to equations **(6)** and **(7)**)
 446 remains phenomenologically unchanged. In other words, a $p < 1$ value cannot be explained by
 447 stress relaxation, whose sole effect is to reinforce the velocity decay, *i.e.* to increase the apparent
 448 p -value. In our case, this suggests that the postseismic deformation during the first month after
 449 the coseismic rupture only marginally relaxed the induced stresses.

450

451 3.1.4 Combination of Viscoelastic Relaxation and Afterslip

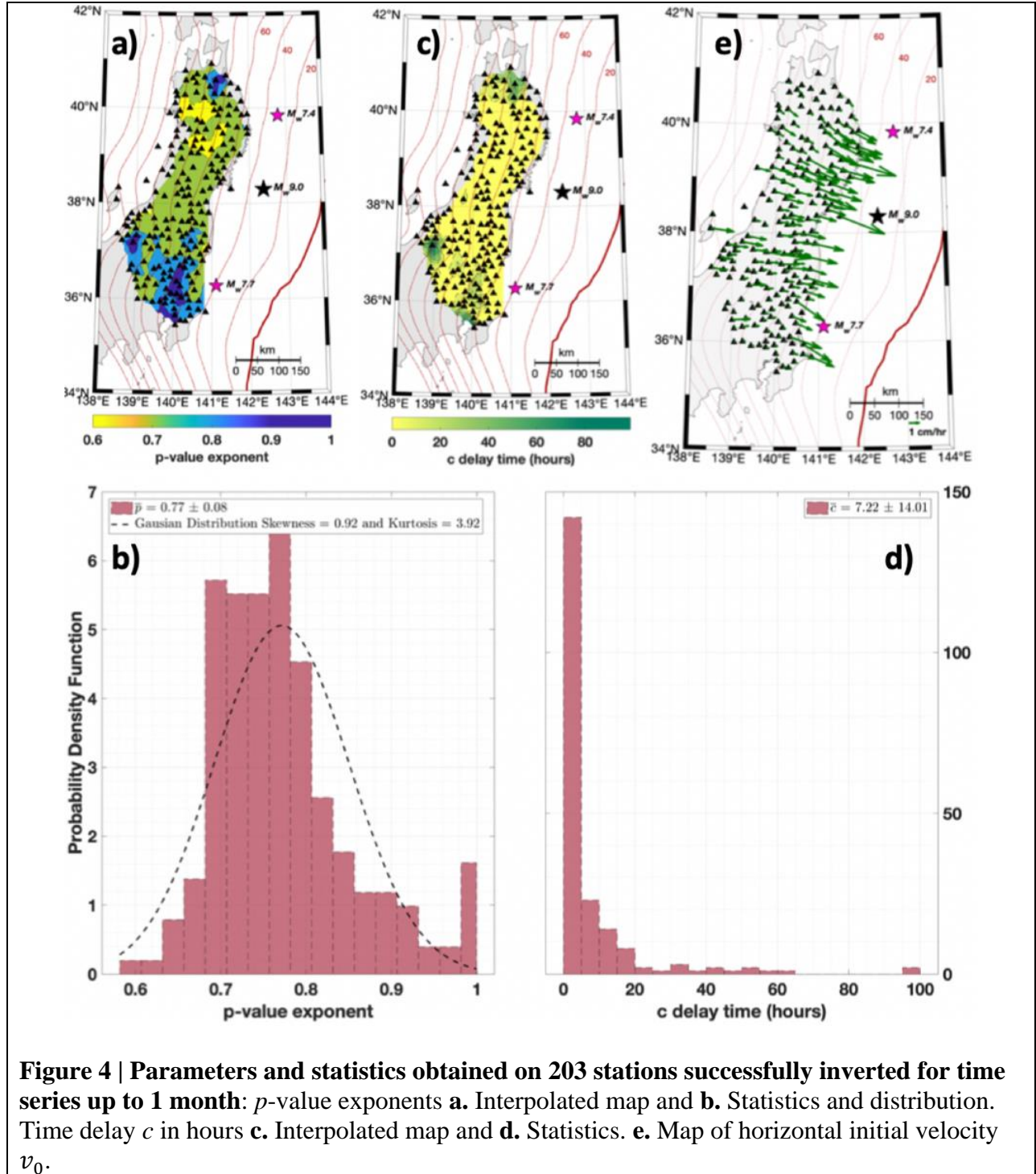
452

453 To complete this analysis, we also considered a mixed model, combining a viscoelastic
 454 mechanism as described by equation **(2)** or **(4)** with afterslip along a “creeping” section of the
 455 fault associated to a logarithmic increase of the surface displacements (expression **(7)**). As we
 456 already described in the previous sections, this $1/t$ decay could be related to a velocity-
 457 strengthening rate-and-state rheology, (expressions **(5)**, **(6)** and **(7)**) or to the cumulative effect of
 458 numerous stress and thermally-activated fracturing and faulting local events (equation **(8)** with
 459 the particular case $p=1$),

$$460 \quad u(t) = v_0 c \ln \left(1 + \frac{t}{c} \right) + v_1 \tau_K \left(1 - e^{-\frac{t}{\tau_K}} \right) \quad \mathbf{(11)}.$$

461

462 This last tested model (green curves on Figures 2-3) is able to properly fit our GPS kinematic
 463 time series, including the first ~forty hours, better than the logarithmic decay model alone
 464 (equation **(7)**). The RMS computed on the residual’s analysis of equation **(11)** (Figure 3) is
 465 similar to the value obtained for the transient brittle creep equation **(10)**. However, we rejected
 466 this model for two reasons. First, the obtained relaxation times τ_K or τ_* (**(2)** or **(4)**) for this
 467 combined model are very short, of the order of a few days. Using a Young’s modulus of $G_K = 50$
 468 GPa, this would imply Kelvin viscosities of the mantle η_K to be of the order of 10^{16} Pa.s, *i.e.*
 469 about 50 times smaller than commonly considered values (Wang et al., 2012). In addition, a
 470 conceptual model involving a single mechanism is always preferable to a more complex one
 471 combining different mechanisms.



472
473
474
475
476
477
478
479
480
481

Figure 4 | Parameters and statistics obtained on 203 stations successfully inverted for time series up to 1 month: p -value exponents **a. Interpolated map and **b**. Statistics and distribution. Time delay c in hours **c**. Interpolated map and **d**. Statistics. **e**. Map of horizontal initial velocity v_0 .**

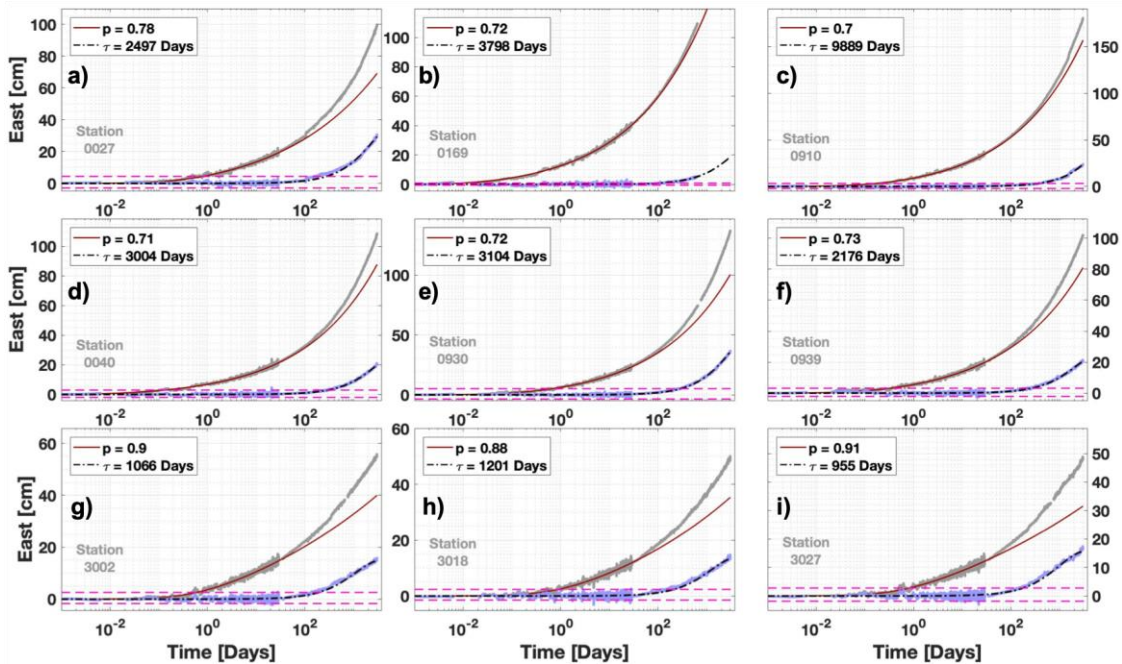
482 3.2 Postseismic Deformation at larger time-scales

483

484 We have shown above that a transient brittle creep model with $p < 1$ fits very well our early
 485 postseismic data, from a few minutes to one month after the mainshock. The following question
 486 is to determine to what extent such model can adequately explain postseismic deformation over
 487 longer timescales. To check this, we used position time series combining our kinematic (30-s)
 488 first-month time series with daily solutions extending up to ~ 9 years after the mainshock. At
 489 each station, the Omori-like decay (equation (10) for displacements) over this longer period
 490 shows a detectable deviation starting ~ 100 days after the Tohoku-Oki earthquake (Figure 5).
 491 This indicates that a transient brittle creep mechanism along the fault cannot account alone for
 492 postseismic deformation at timescales from several months to several years. On Figure 5, we
 493 show that an exponential (equation (4)) adequately fits the residuals of this transient creep
 494 creep model. This suggests a signature of a viscoelastic deformation of the mantle. Thus, we build a
 495 model that combine a transient brittle creep and a viscoelastic deformation of the mantle:

$$496 \quad u(t) = \frac{v_0 c}{1-p} \left[\left(1 + \frac{t}{c}\right)^{1-p} - 1 \right] + v_1 \tau_* \left(1 - e^{-\frac{t}{\tau_*}}\right) \quad (11).$$

497



498

499

500

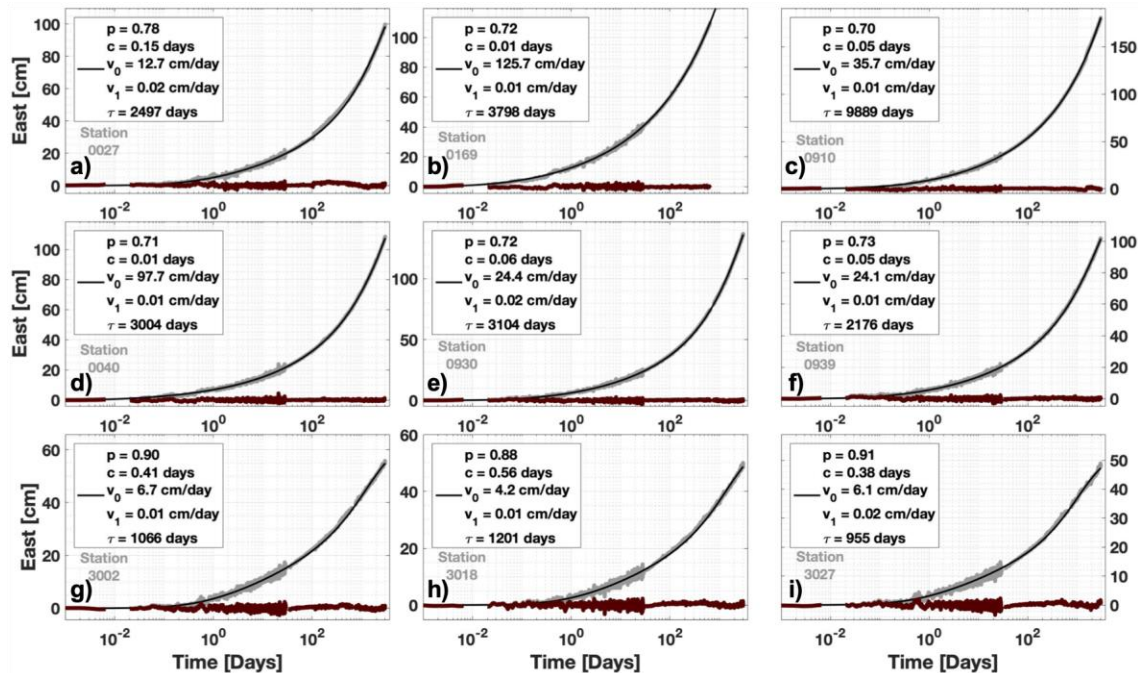
501 **Figure 5 | Residuals Analysis of transient brittle creep model on the combination of GPS**
 502 **kinematic (over one month), + static time series up to ~ 2020 . a-i.** Displacement evolution on
 503 the East component (grey curve) during ~ 9 years after the mainshock in logarithmic scale on the
 504 x-axis. The p -value of the transient brittle creep (equation (10) - red curves) was determined over
 505 the first month. Then, the related residuals displacements are computed (blue curves) over large
 506 timescales.

507 The black dashed-dotted curves correspond to equation (2) or (4). RMS of residual

508 displacements is shown (magenta dotted lines). Stations locations are represented on **Figure 1b**

509 (grey triangles) and situated **a-c**. Near the coast of Tohoku **d-f**. Center of Japan **g-i**. Near the
 510 coast of Ibaraki.

511
 512

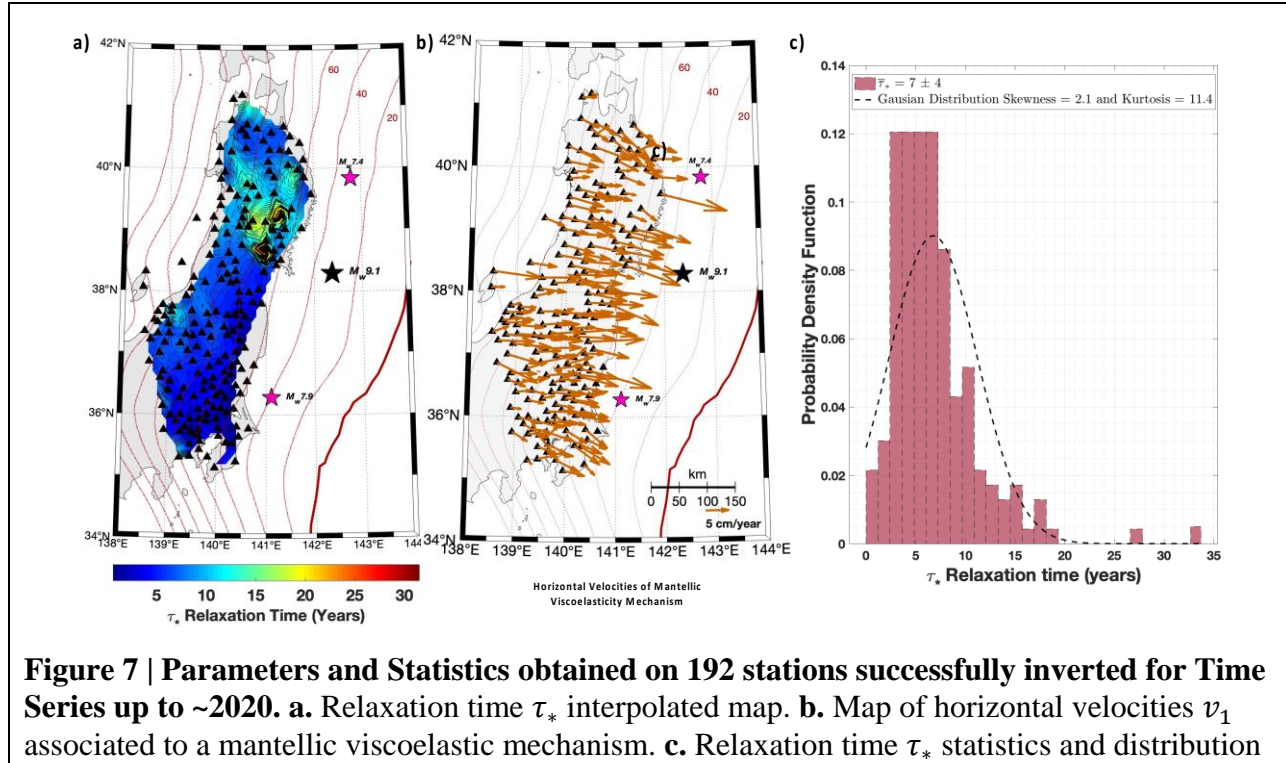


513
 514

515 **Figure 6 | Temporal Evolution and models used to fit GPS kinematic + static time series up**
 516 **to ~2020. a-i.** Displacement evolution on the East component (grey) during ~9 years after the
 517 mainshock in logarithmic scale on the x-axis. The transient brittle creep mechanism determined
 518 by a p -value is combined with an exponential decay function associated to a mantellic
 519 viscoelastic mechanism (equation (2) or (4)) which the nature is debated in the discussion (black
 520 curves). Final residual displacements (brown curves). Station locations are represented on
 521 Figure 1b (grey triangles) and situated **a-c**. Near the coast of Tohoku **d-f**. Center of Japan **g-i**.
 522 Near the coast of Ibaraki.

523
 524

525 Figure 6 shows how well this model explains our data from 10 minutes after the mainshock up to
 526 several years after. Here v_0 , c and p have been obtained from our kinematic time series over the
 527 first month (section 3.1.3), while v_1 and the characteristic time τ_* have been determined from a
 528 similar non-linear least square inversion method on the residuals shown on Figure 5 (blue
 529 curves). Results are shown on Figure 6 (black curves). We explored the spatial variations on the
 530 relaxation time τ_* (see Figure 7a) and we observed a relaxation time around 7 years (statistics on
 531 Figure 7b), and which seems to be larger near the Tohoku-Oki earthquake. We have also
 532 explored the spatial variations of v_1 on Figure 7c and we find velocities v_1 of a few cm/year,
 533 which is orders of magnitude lower than the few cm/hr of the initial postseismic velocities v_0
 534 obtained for the afterslip component. Considering a negligible stress relaxation and a shear
 535 modulus of $G_K = 50$ GPa, a characteristic timescale of ~7 years would yield a viscosity around
 536 10^{19} Pa.s where the spatial variations of η_* are available on Figure S4. This is compatible with
 537 the values of the Maxwell viscosity reported in the literature (Sun et al., 2014).



538
539
540
541
542

Figure 7 | Parameters and Statistics obtained on 192 stations successfully inverted for Time Series up to ~2020. a. Relaxation time τ_* interpolated map. **b.** Map of horizontal velocities v_1 associated to a mantellic viscoelastic mechanism. **c.** Relaxation time τ_* statistics and distribution

543 To conclude on the temporal evolution of the postseismic surface displacements after the
544 Tohoku-Oki earthquake, we observe that the kinematic position time series during the first
545 month following the earthquake are well explained with a transient brittle creep model, with a p
546 exponent of about 0.75 on most of the region and a p exponent closer to 1 on the south nearby
547 the Ibaraki-Oki aftershock. This temporal evolution differs from the $1/t$ decay (*i.e.* $p=1$)
548 predicted by velocity-strengthening friction. Over longer time scales (several years), an
549 additional mechanism, compatible with viscoelastic mantle relaxation has to be considered.
550 In the following, we investigate in more details the first month of the postseismic phase, and
551 focus on its spatial pattern. In addition to the spatial variability in the p -value already discussed,
552 we will estimate the location of the aseismic slip on the plate interface.
553

554 4 Static Inversion to constrain coseismic and postseismic slip

555

556 In what follows, we consider that the postseismic signal occurring during the first month after the
557 earthquake is due either to frictional sliding on the plate interface or shear on a localized band
558 around the interface, and we estimate its spatial distribution by inverting the GPS data (see
559 details Text S1). We invert East and North components as well as Vertical component even if it
560 is associated to larger uncertainties. In Japan, the large number of inland stations allows to
561 estimate with a good spatial resolution the occurrence of slip below the island. However, the
562 resolution is poor in the offshore region of the plate interface (see Text S2 and Figure S5). Using
563 the configuration detailed in Figure S6a-b we estimate the slip on the plate interface by doing
564 static inversions for 12 successive time windows.
565

566 4.1 Time windows definition

567
 568 We estimate the postseismic displacements over the first month for several time windows with
 569 increasing duration, and select the time windows so that they correspond to a similar increase in
 570 surface displacement. We use the station 0930 as a reference, since it records among the largest
 571 postseismic displacements. The cumulative displacement windows $\Delta d = 2, 4, 6, \dots$ cm define
 572 time windows $[t_0^*, t_0^* + \Delta t]$ of increasing duration from 3.25 hours to 29.4 days, see details in
 573 Figure S7. We end up separating the first month of postseismic record into 12-time windows,
 574 each corresponding to an almost identical amplitude of displacement, as shown in Figure S7. As
 575 the postseismic velocity decreases with time, the successive time-windows have an increasing
 576 duration. Then, we perform static inversions for the co-seismic displacements of the Tohoku-Oki
 577 and Ibaraki-Oki events, as well as for the cumulative post-seismic displacement over these
 578 different time windows.
 579

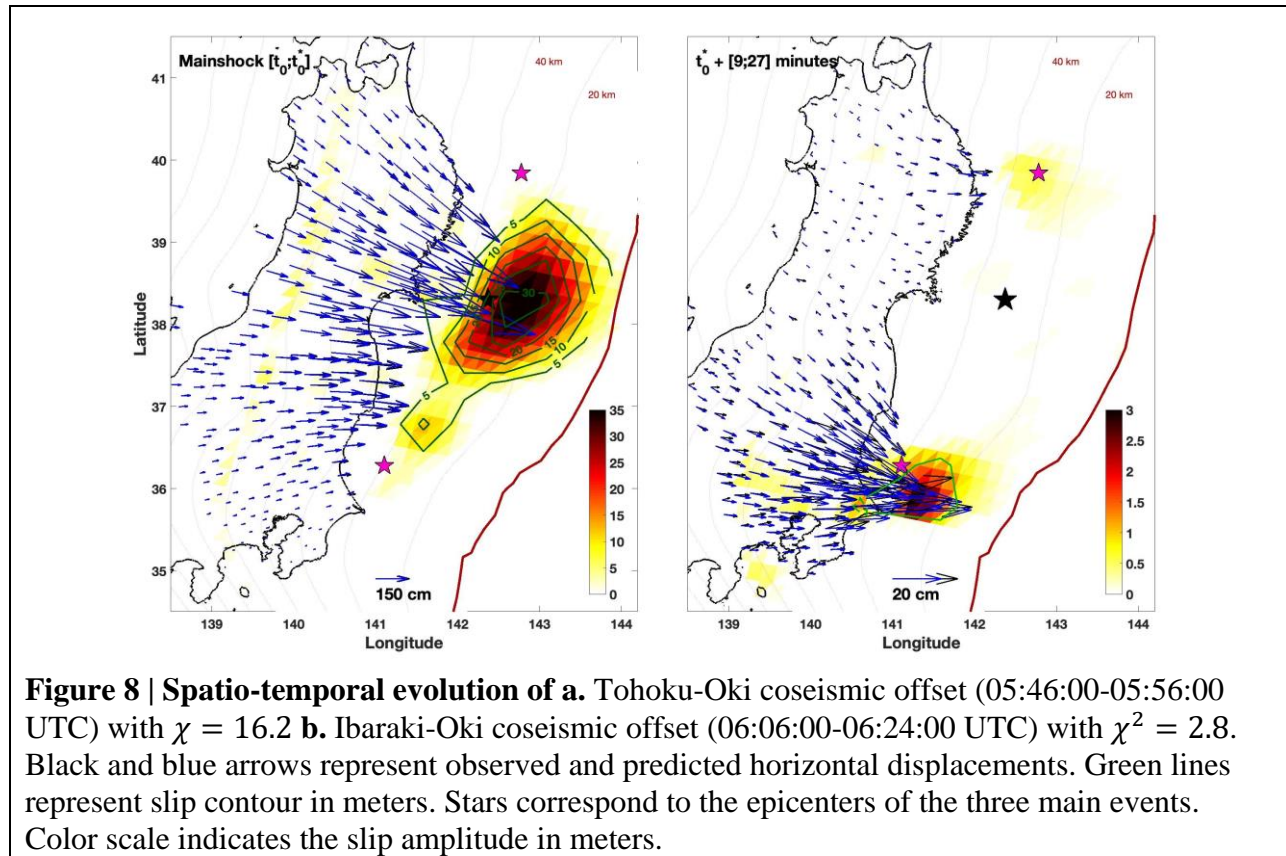
580 4.2 Slip inversion procedure

581
 582 For each time window considered, the horizontal and vertical displacements are inverted to
 583 estimate the slip on the subduction interface. We inverted East and North components as well as
 584 the Vertical component associated to large uncertainties (computed on time series in Section 2).
 585 We use the 3D geometry from Slab 2.0 (Hayes et al., 2018) to represent the Japanese subduction
 586 interface. The slab extends about 600 km along strike and 350 km along dip, down to a depth of
 587 110 km. It is discretized in 1526 triangular patches of $\sim 193 \text{ km}^2$. The static Greens functions are
 588 computed for an elastic half space using (Okada, 1992). We use a regularized least square
 589 inversion scheme following (Radiguet et al., 2011, 2016) (see details in Text S1). The selection
 590 of the optimal slip directions and regularization parameters is detailed in the Figure S6a-b.
 591

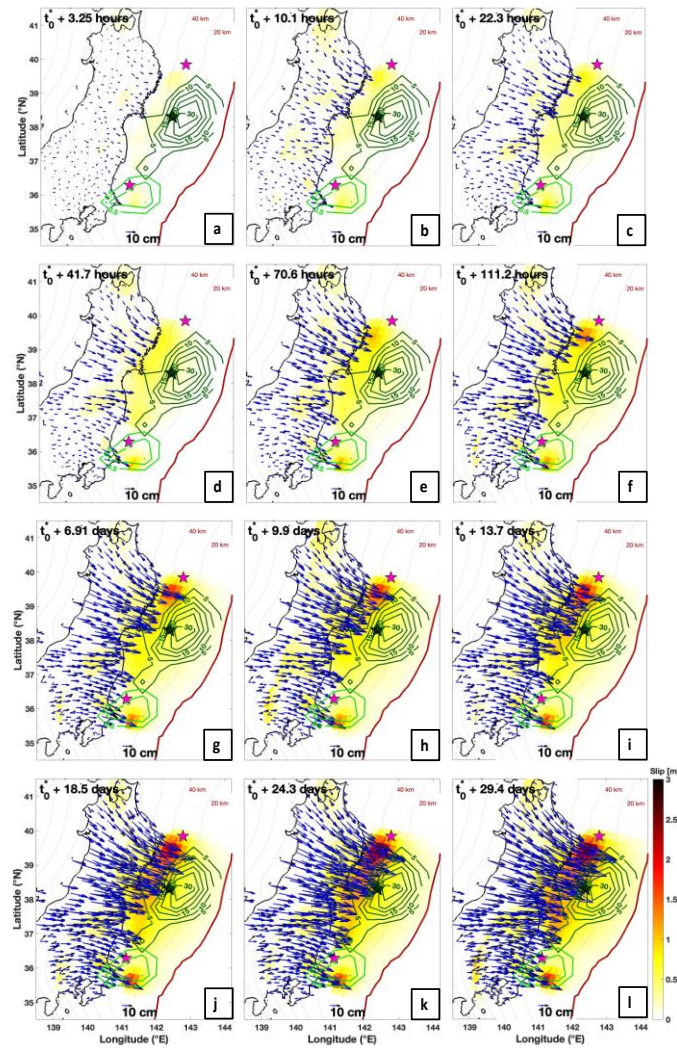
592 4.3 Slip location for the mainshock, aftershocks and the early postseismic period

593
 594 The slip models obtained for the mainshock and aftershocks coseismic displacements are shown
 595 on Figure 8a and 8b (see residual horizontal displacements Figure S8). The mainshock coseismic
 596 slip distribution has a moment magnitude of M_w 9.0 (assuming a Young Modulus $E=50 \text{ GPa}$),
 597 and corresponds to a large area of shallow ($<30 \text{ km}$) slip near the trench with a maximum
 598 amplitude of ~ 33 meters. This model, although constrained only by onshore GPS stations, gives
 599 a first order estimate of the co-seismic offset slip distribution for the Tohoku-Oki earthquake.
 600 Our model is consistent with several previously published models, but probably underestimates
 601 the large amount of slip close to the trench since we use only onshore GNSS data (see for a
 602 review (Lay, 2018; Tajima et al., 2013; Wang et al., 2018)). The inversion of the time window
 603 which includes the aftershocks, see below, (Figure 8b) $[t_0^*+9 \text{ min} - t_0^*+27 \text{ min}]$ allows to
 604 estimate the slip distribution which corresponds to a magnitude of M_w 7.9. We identified a first
 605 slip region nearby the Ibaraki prefecture which is associated to the aftershock of Ibaraki-Oki
 606 (06:15:34 UTC) which has a magnitude of M_w 7.7 (F-NET) or M_w 7.9 (USGS). We also
 607 remarked a small slip dip area north of Tohoku-Oki which corresponds to the location of a M_w

608 7.4 (06:08:53 UTC) aftershock (identified by F-NET), that occurred during the same 18 minutes
 609 time window.
 610



611
 612
 613
 614
 615
 616
 617
 618 To explore the postseismic period, we remove the aftershocks coseismic offsets, estimated by a
 619 step function, from the time series. We represent the cumulative (since t_0^*) slip distribution
 620 during the first month of the postseismic period, for the 12-time windows of increasing duration
 621 (see Figure 9 and residual horizontal displacements Figure S9), as defined in Section 4.1. For the
 622 first snapshot (Figure 9a, $t_0^* + 3.25$ hours), the signal is slightly above the noise level (maximum
 623 2 cm of displacement at some stations), and it is difficult to distinguish a clear pattern in the slip
 624 distribution, although the slipping area is located downdip the mainshock (a distribution that is
 625 potentially biased by the lack of resolution nearby the trench). The successive snapshots for the
 626 first day (Figure 9b-c) reveal a coherent trenchward motion of the GPS network. Our inversion
 627 reveals two main afterslip regions: one located just below the Tohoku-Oki co-seismic slip
 628 rupture, and a second one south of the Ibaraki-Oki aftershock, while between these 2 regions, an
 629 intermediate zone at the latitude $\sim 37^\circ\text{N}$ (see Figure 9d-l) do not show significant afterslip. The
 630 existence of these two well-separated patches of afterslip is actually visible in the pattern
 631 displayed by the surface GPS displacements, characterized by two groups of GPS stations
 632 pointing towards two distinct directions. The amount of postseismic surface displacements and
 633 corresponding afterslip for the first day after the event, shown in Figure 9 a-c is not available
 634 using daily GPS solution alone. We can see that this first day early afterslip is significant, with
 635 maximum horizontal displacements of 18 cm, corresponding to an equivalent magnitude of M_w 8
 636 for the whole subduction interface (see Figure 10.a-b).

637
638

639 **Figure 9 | Spatio-temporal evolution of afterslip during the first month on 12-time**
 640 **windows:** Aftershock(s) coseismic offsets are removed from the postseismic deformation. Black
 641 and blue arrows represent observed and predicted horizontal displacements. Green lines
 642 represent slip contours of the Tohoku-Oki mainshock and Ibaraki-Oki aftershock in meters. Stars
 643 correspond to the three main events. Color scale indicates the slip amplitude in meters.

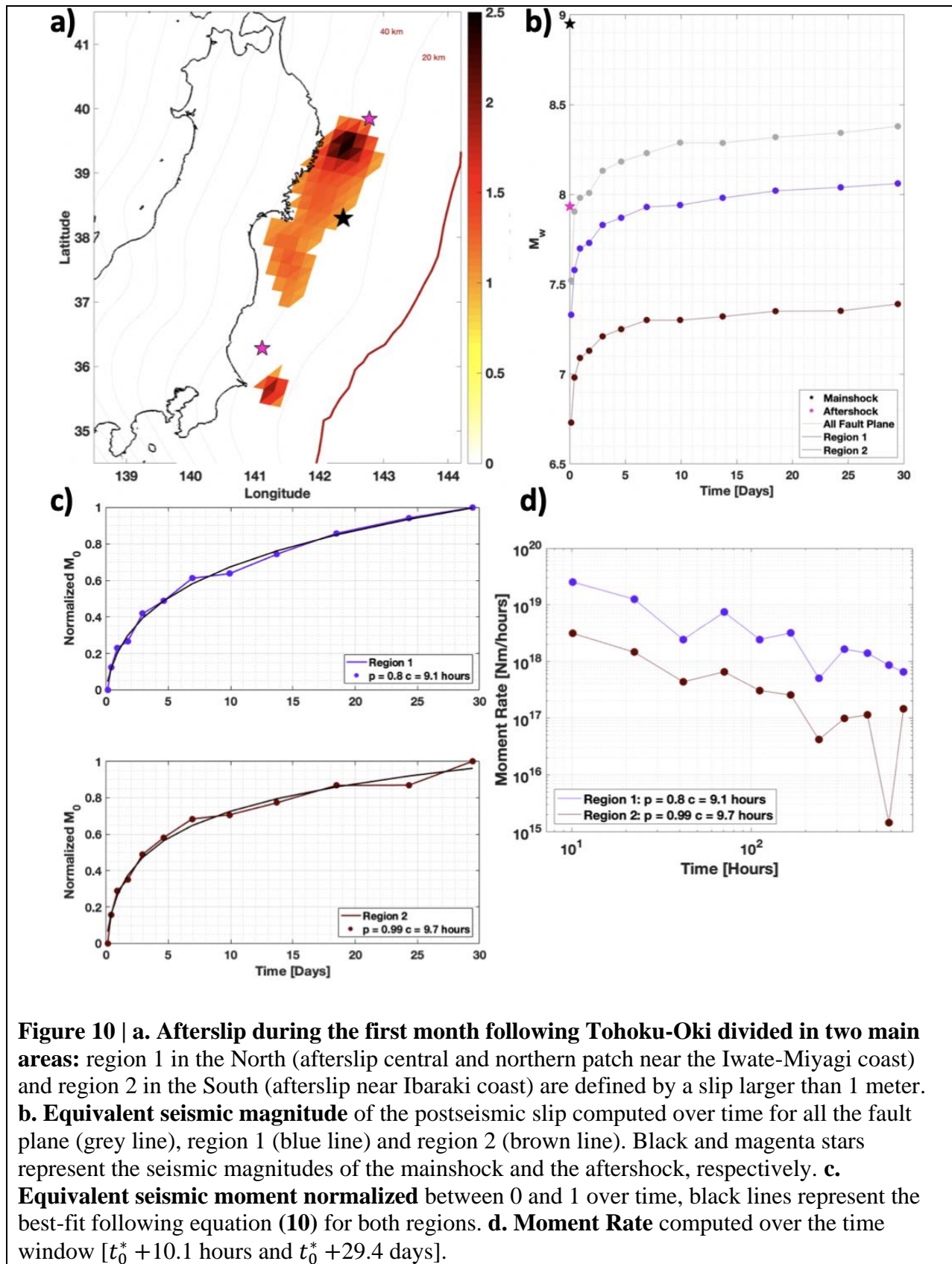
644 **a.** $t_0^* + 3.25$ hours and $\chi^2 = 7.2$. **b.** $t_0^* + 10.1$ hours and $\chi^2 = 4.1$. **c.** $t_0^* + 22.3$ hours and
 645 $\chi^2 = 25.5$.

646 **d.** $t_0^* + 41.7$ hours and $\chi^2 = 39.4$. **e.** $t_0^* + 70.6$ hours and $\chi^2 = 18.2$. **f.** $t_0^* + 111.2$ hours and
 647 $\chi^2 = 11.2$

648 **g.** $t_0^* + 6.91$ days and $\chi^2 = 54.0$. **h.** $t_0^* + 9.9$ days and $\chi^2 = 27.6$. **i.** $t_0^* + 13.7$ days and
 649 $\chi^2 = 41.1$.

650 **j.** $t_0^* + 18.5$ days and $\chi^2 = 43.4$. **k.** $t_0^* + 24.3$ days and $\chi^2 = 73.8$. **l.** $t_0^* + 29.4$ days and
 651 $\chi^2 = 9.5$.

652 Our slip inversion shows that the largest amplitude of the early afterslip is located mostly at
653 depth between 30 and 50 km, downdip of the coseismic slip, and is separated in two patches
654 (region 1 and region 2 in Figure 10a), in agreement with previous studies (see for a review (Lay,
655 2018; Tajima et al., 2013; Wang et al., 2018)). Our inversion also shows some afterslip of lower
656 amplitude propagating in the coseismic rupture zone. Given the low resolving power of our
657 onshore GNSS data to offshore slip (see Text S2 and Figure S5), we consider that this feature is
658 not well resolved. A robust pattern is the identification of two main afterslip regions, one located
659 just below the mainshock and another one on the south, associated to the M_w 7.7 aftershock,
660 separated by a region of low afterslip (Figure 10a). We postulate that these two regions could be
661 associated with the different temporal evolutions identified in the previous section. We estimate
662 the equivalent seismic moments and magnitudes released aseismically for these two regions
663 (Figure 10b-c) and their associated moment rates (Figure 10d). As expected, region 1 (below the
664 mainshock) has a larger magnitude than region 2 (M_w 8.1 versus M_w 7.4 after 1 month). Despite
665 the low temporal resolution of our kinematic inversion (12 sequences over 1 month), a fit to the
666 temporal evolution of the cumulative moment using equation (10) gives an optimal p value of 0.8
667 for region 1 and 0.99 for region 2, which is compatible with the models from in the previous
668 section obtained using the position time series (with $p \sim 0.75$ in region 1 and $p \sim 1$ in region 2), and
669 confirms the differences in the temporal evolution of afterslip for the two regions.
670



671
672
673
674
675
676
677
678
679
680
681

Figure 10 | a. Afterslip during the first month following Tohoku-Oki divided in two main areas: region 1 in the North (afterslip central and northern patch near the Iwate-Miyagi coast) and region 2 in the South (afterslip near Ibaraki coast) are defined by a slip larger than 1 meter. **b.** Equivalent seismic magnitude of the postseismic slip computed over time for all the fault plane (grey line), region 1 (blue line) and region 2 (brown line). Black and magenta stars represent the seismic magnitudes of the mainshock and the aftershock, respectively. **c.** Equivalent seismic moment normalized between 0 and 1 over time, black lines represent the best-fit following equation (10) for both regions. **d.** Moment Rate computed over the time window $[t_0^* + 10.1$ hours and $t_0^* + 29.4$ days].

682 **5 Discussion**

683

684 The former observations of early postseismic deformation following large subduction
 685 earthquakes were limited by the low number of GPS time series (Twardzik et al., 2019). The
 686 Tohoku-Oki earthquake studied in this paper represents an opportunity to improve our
 687 understanding of such postseismic phase and to constrain its temporal evolution over a wide
 688 range of timescales (Malservisi et al., 2015), owing to the large aseismic displacement recorded
 689 and the dense network of GPS stations. In Section 3, we argued that our GPS time series, from
 690 the timescale of a few minutes to that of several years after the coseismic rupture can be
 691 explained by a combination of afterslip, largely dominant at short timescales, and a viscoelastic
 692 relaxation process of the mantle at longer timescales. Hereafter we mainly discuss the nature of
 693 the afterslip mechanism, which dominates the early postseismic stage with an Omori-like
 694 signature (Figure 2). Its temporal evolution mostly depends on the p -value (equation (10)) which
 695 we found, consistently with (Morikami & Mitsui, 2020), to be significantly smaller than 1 except
 696 for a small region near the Ibaraki-Oki aftershock where the p -value is closer to 1 (Figure 4a).
 697 We have highlighted that this $p < 1$ value is incompatible with a classical velocity-strengthening
 698 regime of a rate-and-state rheology. Hereafter we propose a possible mechanism to explain p
 699 values lower than 1, which we attempt to validate using numerical mechanical modelling.

700

701 **5.1 Velocity-Strengthening interfacial rheology versus Transient Brittle Creep**

702

703 As we already mentioned above, the current interpretations of afterslip are either based on a
 704 velocity-strengthening regime of a rate-and-state rheology for a frictional interface (Marone et
 705 al., 1991; Perfettini & Ampuero, 2008; Perfettini & Avouac, 2004), or a transient creep
 706 mechanism (Savage, 2007; Savage et al., 2005). Although these two interpretations appear at
 707 first glance as being different in nature, they actually share some similarities in their underlying
 708 physics. Scholz modeled transient brittle creep as resulting from the cumulative effect of
 709 numerous stress- and thermally-activated fracturing events, (Scholz, 1968) each of them
 710 inducing a small strain/slip increment, and predicted a logarithmic strain (or slip) of the type
 711 $\varepsilon(t) \sim \ln(1 + \frac{t}{\tau})$, corresponding to a strain-rate (or slip velocity) decaying in $\frac{1}{t}$, *i.e.* $p=1$. In other
 712 words, this approach is unable to model the $p < 1$ values characterizing the early phase of afterslip
 713 for the Tohoku earthquake in most regions (Figure 4.a). However, Scholz's model, reconsidered
 714 more recently by Savage and co-workers in the context of post-seismic deformation (Savage,
 715 2007; Savage et al., 2005), is based on several strong simplifying assumptions:

- 716 (i) An exhaustion hypothesis, *i.e.* a local site/asperity cannot slip more than once
- 717 (ii) An absence of mechanical interactions between slip events

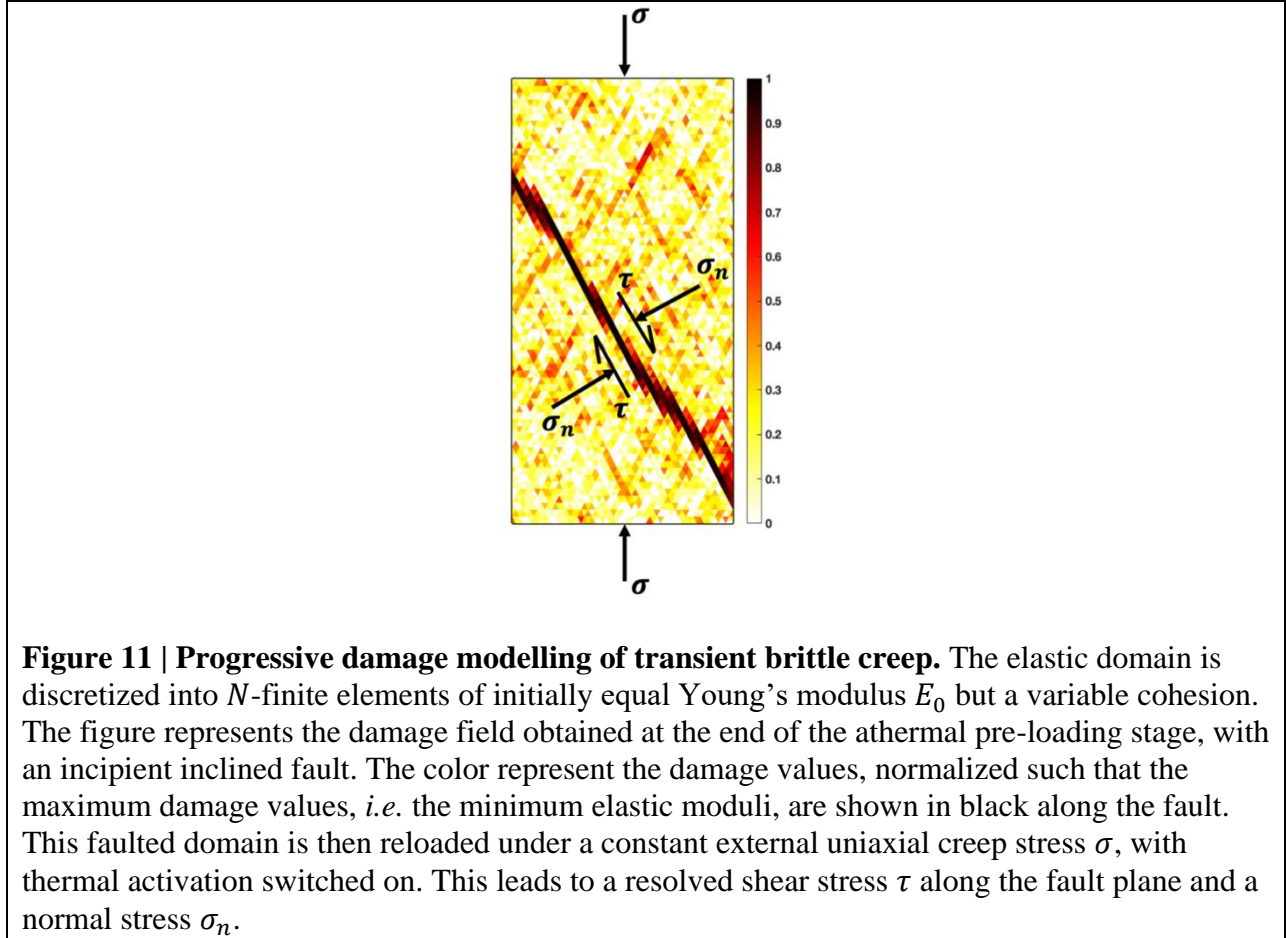
718 On the other hand, the rate-and-state rheology originates from an empirical formulation based on
 719 laboratory sliding-block experiments (Dieterich, 1979; Marone, 1998). (Baumberger et al., 1999;
 720 Heslot et al., 1994) considered the role of thermal activation of local slip events to explain the
 721 velocity-strengthening regime of dynamic friction, as well as the aging of the interface under
 722 constant normal stress (the state effect). This suggests a similarity with brittle creep. However,

723 much like in Scholz's model of brittle creep, they neglected elastic interactions between
724 microslip events.

725 As we will show in Section 5.2, these simplifying assumptions are unphysical, and their release
726 allows modeling a transient creep with p -values lower than 1, as well as possible effect of
727 temperature on the p -value.
728

729 5.2 Transient Brittle Creep as a combination of thermally-activated processes and elastic stress 730 transfers

731
732 To explore this, we used a damage model, which takes into account elastic interactions, and
733 implemented thermal activation from a kinetic Monte-Carlo algorithm (Bortz et al., 1975). The
734 athermal version of this damage model has been thoroughly detailed elsewhere (Amitrano et al.,
735 1999; Girard et al., 2010), hence we will only recall its main characteristics here. In this 2D
736 model (see Figure 11), an elastic domain is discretized into N finite-elements, all with the same
737 Young's modulus E_0 . Loading is applied on the boundaries of the domain. Initial disorder is
738 introduced from a spatially variable cohesion drawn from a uniform distribution. At the element
739 scale, damage of the material, i.e a decrease of the modulus E by a factor $1-d$ (with $d=0.1$ for the
740 simulations presented below), occurs whenever the local stress state reaches a Mohr-Coulomb's
741 criterion (see Figure S10). This local softening generates a strain increment. After each damage
742 event, the static equilibrium is re-calculated while the external loading is maintained constant,
743 inducing a redistribution of elastic stresses within the domain, which can potentially trigger
744 additional damage events, particularly in the vicinity of the former one (see details in Figure
745 S10). This was shown to successfully reproduce the main characteristics of rocks damage and
746 Coulombic failure, such as the progressive localization of damage upon approaching a peak
747 stress at which an incipient fault nucleates, or the impact of confining pressure and of the internal
748 friction μ on strength and on the mechanical behavior (ductile vs brittle) (Amitrano, 2003;
749 Amitrano et al., 1999). This way, our model physically considers elastic interactions between
750 damage/strain events, *i.e.* releases the assumption (ii) of Scholz's model mentioned above. In
751 addition, a given element can damage several times in the course of deformation, hence releasing
752 the exhaustion assumption (point (i) above). Such cascades of events eventually explain damage
753 and strain localization along a "fault". There is no explicit timescale in the athermal version of
754 the model, which is therefore unable to simulate creep deformation under a constant external
755 loading. (Amitrano & Helmstetter, 2006) introduced time-dependent damage within this
756 framework from deterministic static fatigue laws at the element scale. This allowed to
757 successfully reproduce the phenomenology of creep of rocks, including the transition from stage
758 I (a decelerating creep) to stage III (an accelerating creep) preceding failure.
759



770

771

772 We consider here a different approach based on a stochastic, physics-based modeling of thermal
773 activation. In the athermal model, damage can only occur when the local stress state reaches the
774 Mohr-Coulomb failure envelope. In this new version, at any time t a damage event can occur at
775 element i , with a probability:

776

$$P_i \sim \exp\left(\frac{-E_a^i}{k_B T}\right) \quad (12),$$

777

778

779

where $k_B = 1.38 \cdot 10^{-23} \text{ J.K}^{-1}$ is the Boltzmann constant, T the temperature, and E_a^i an activation energy of damage for the element i in J. A natural choice for this activation energy is (Castellanos & Zaiser, 2018):

780

$$E_a^i = V_a \Delta\sigma_i \quad (13),$$

781

782

783

784

785

786

787

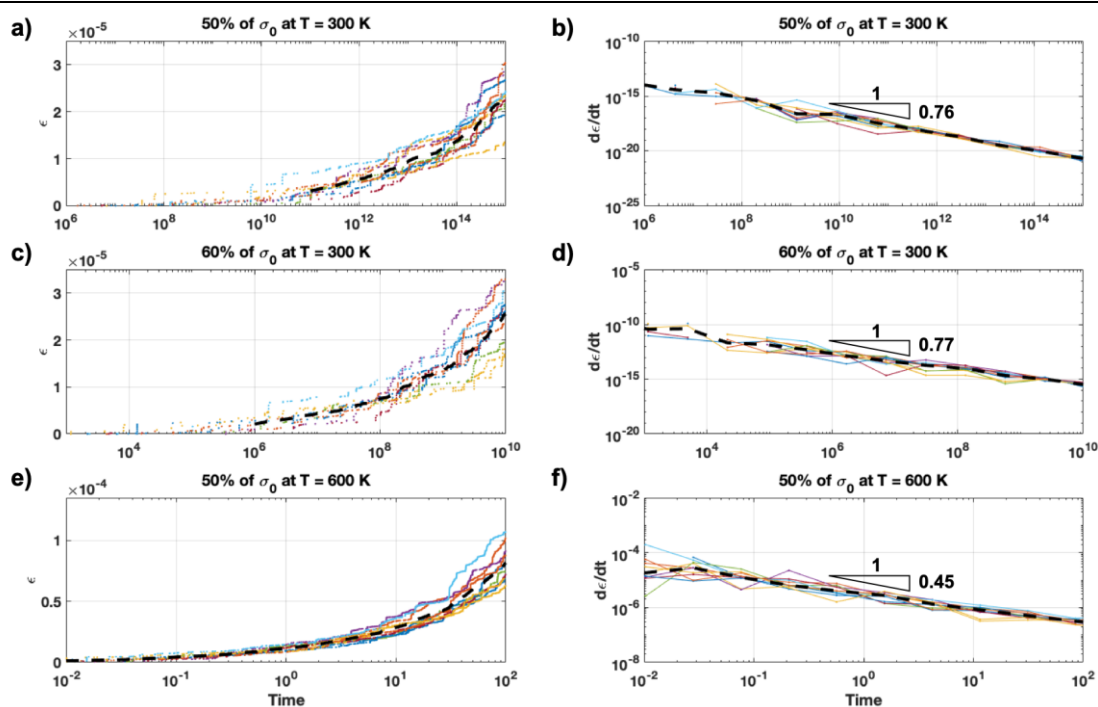
788

789

where V_a is a spatially constant activation volume and $\Delta\sigma_i$ a Coulomb stress gap between the stress state of the element i at time t and the Mohr-Coulomb failure envelope. The kinetic Monte-Carlo algorithm allows to randomly select in an efficient numerical way, following a probability P_i , the element i that will damage next after a Δt_i time delay. This is not necessarily the one which is the nearest from its local damage threshold, although its probability of damage is the largest (12). As soon as a damage event is thermally activated, elastic stresses are redistributed without advancing further the time (the corresponding elastic timescales are considered to be negligible compared to those of thermally-activated creep), and possibly trigger new damage events in an athermal way. Once such an athermal cascade stops, a new thermally activated event

790 j is selected and time increases by Δt_j . This way, the model combines thermally-activated
 791 damage and deformation as well as elastic stress redistributions. In what follows, the values of V_a
 792 and T , as well as the distribution of local cohesion values have been chosen arbitrarily. Indeed,
 793 we are not interested in predicting quantitatively creep kinematics for some specific material,
 794 instead in simulating the phenomenology of transient creep.
 795

796 To do this, we considered the following loading protocol (see details in Figure S10). The internal
 797 friction coefficient is fixed to $\mu=0.7$. A rectangular domain is first compressed uniaxially under a
 798 monotonic and *athermal* way, following previous works (Amitrano et al., 1999; Girard et al.,
 799 2010). This leads to the development of an inclined fault of highly damaged material, associated
 800 to a large macroscopic stress drop. We stop this preliminary step just after this stress drop, and
 801 unload the domain. The resulting damage pattern then serves as an initial condition (see Figure
 802 S10) for a second step. During that second step the kinetic Monte-Carlo algorithm is switched on
 803 and the domain is re-loaded under a constant macroscopic uniaxial compression stress σ_0 (creep
 804 mode) corresponding to some % of the stress remaining after the stress drop of step 1. This way,
 805 we simulate the creep of a pre-damaged fault under both normal and shear stress components
 806 along the fault plane. In this configuration, all damage and deformation accumulating during the
 807 transient creep loading concentrates along the pre-existing fault, while the upper and lower
 808 blocks mimic the role of much stiffer elastic plates, however allowing elastic stress transfers. All
 809 the results summarized below have been average over 10 realizations of the initial disorder (see
 810 Figure 12).
 811



812
813

814 **Figure 12 | Strain ϵ (left) and Strain Rate $\frac{d\epsilon}{dt}$ (right) obtained for the creep deformation of**
 815 **the modelled domain, with the following modelling parameters: Friction coefficient $\mu = 0.7$,**
 816 **constant loading maintained at 50% or 60% of the stress remaining after the stress drop of the**

817 pre-loading stage, for $T = 300\text{ K}$ (a-d) or $T = 600\text{ K}$ (e-f). Ten simulations corresponding to
 818 different realizations of the initial disorder were performed in each case, and the black dotted
 819 curves represent the average response where the slopes represent the p -values estimated. The
 820 present curves focus on the transient creep (stage I).

821
 822 The resulting macroscopic strain $\varepsilon(t)$ and strain-rate $\dot{\varepsilon}(t)$, which can therefore be directly linked
 823 to a displacement and average “slip velocity” along the fault, follows the typical phenomenology
 824 of rocks creep with a decelerating primary (or transient) creep stage I (see Figure 12 b,d,f)
 825 followed by an accelerating stage III (see Figure S11). Note that, in our simulations and much
 826 like what is observed in rocks, the creep stage II associated to a supposedly constant strain-rate
 827 $\dot{\varepsilon}_{min}$ seems to manifest only in the form of an inflection point (see Figure S11). We are not
 828 interested here in the accelerating stage III, which resulted in our simulations from the
 829 development of a secondary conjugate fault, and focus instead on the transient stage I (see Figure
 830 12 b,d,f) during which all deformation occurs along the pre-existing fault (see Figure S10). Note
 831 that under a slow constant strain-rate loading condition, more consistent with tectonic loading at
 832 large timescales, such accelerating creep (stage III) would not occur as the primary creep would
 833 relax the stress.

834 In our simulations, the transient creep (stage I) is characterized by a power-law decay of the
 835 strain-rate, $\dot{\varepsilon}(t) \sim 1/t^p$, with a p -value always smaller than 1, over several orders of timescales
 836 (Figure 12). We can therefore conclude that a transient brittle creep mechanism combining the
 837 thermal activation of damage/strain/slip events as well as elastic stress interactions allows
 838 reproducing the phenomenology of Tohoku early afterslip. This can be qualitatively interpreted
 839 as follows: a p -value smaller than 1 implies a slower decay of the afterslip rate compared to $p=1$.
 840 This comes from the fact that, unlike for the simpler Scholz’s approach, a thermally activated
 841 event can trigger a cascade of athermal events, or the associated stress redistribution can advance
 842 the clock of thermal activation of other sites, in the end sustaining the creep dynamics. In
 843 addition, a given site/asperity can slip several times during afterslip, while Scholz excluded this
 844 possibility with his exhaustion assumption.

845 By increasing the applied creep stress while keeping the temperature T unchanged (see Figure 12
 846 a-b), we observed a shortening of the transient creep stage I (see Figure S11), as expected, but no
 847 significant modification of the p -value. Instead, an increase of temperature T , while keeping the
 848 applied stress constant, appears to decrease the p -value as observed for rocks creep in laboratory
 849 tests (Carter & Kirby, 1978), see Figure 12 a-c.

850

851 5.3 Identification of two main Afterslip regions

852

853 The detailed inversion procedure provides a robust pattern which allow the identification of two
 854 main afterlip regions (Figure 9 and 10a), one below the mainshock and another one, separated by
 855 a zone of lower afterslip, located on the south. This spatial separation (Figure 10) and the
 856 analysis of the temporal evolution of afterslip on the northern and southern region (Figure 2, 4
 857 and 10b), have shown a different behavior defined by a larger p -value on the southern region.
 858 The postseismic deformation recorded in the Southern region is most likely the consequence of
 859 the M_w 7.7 Ibaraki-Oki earthquake, this large aftershock having triggered its own afterslip
 860 sequence which can be detected by the nearby stations. One possible explanation to understand
 861 why afterslip in this region 2 evolves differently with respect to the region 1 could be related to a

862 temperature effect. In the southern region, thermal models (Ji et al., 2016) suggest a negative
 863 thermal anomaly, related with the nearby subduction Philippine sea plate. The results of our
 864 numerical simulations (Figure 12) provide some clues that a lower temperature could have some
 865 impact on the transient brittle creep signature (*i.e.*, higher p -values). This could potentially
 866 explain, at least partly, the larger p -values observed south of 37°N (see Figure 4a).
 867

868 5.4 Postseismic deformation at larger timescales and Viscoelastic Relaxation

869

870 At timescales larger than a few months, transient afterslip is unable to fully explain our
 871 displacement records. We have shown that the associated residuals are characterized by an
 872 exponential decay (figures 5-6), therefore suggesting a combination of transient afterslip and
 873 viscoelastic relaxation in the mantle (see equations (2) and (4)) to explain the entire postseismic
 874 deformation from a few minutes after the coseismic rupture up to several years.

875 As mentioned in Section 3, considering a classical Burgers rheology for the viscoelasticity of the
 876 mantle with two characteristic timescales $\tau_K \ll \tau_M$, such an exponential decay can be explained
 877 either by (i) a transient viscoelasticity regime (associated to τ_K) under a constant stress (equation
 878 (2)), or (ii) the Maxwell component of the rheology (associated to τ_M) relaxing the stress
 879 (equation (4)). The viscosities obtained from our data, around 10^{19} Pa.s, are in favor of the
 880 second explanation.

881 Our analysis did not include the near-trench observations coming from seafloor GPS
 882 measurements, as the first data obtained contain several days of postseismic signal. This is the
 883 major difference with the studies of (Sun et al., 2014; Sun & Wang, 2015). These authors
 884 observed a landward motion of the zone nearby, in opposition with the seaward motions
 885 recorded by the land GPS stations. Considering this near-field observations, they modeled the
 886 postseismic deformation with a transient viscoelastic mantle rheology in the oceanic mantle.
 887 They argued that a non-negligible role of this viscoelasticity leads to a large reduction of the
 888 afterslip required to explain the land GPS data. However, their conclusion is not necessarily in
 889 contradiction with ours, as the period covered by their study is 1 to 3 years after the Tohoku-Oki
 890 earthquake, while we show that afterslip associated to a transient creep mechanism dominates the
 891 postseismic deformation up to few months after the coseismic rupture. Over this early period, we
 892 consider viscoelastic relaxation of the mantle to be negligible to explain the motions of the GPS
 893 stations installed in mainland Japan.
 894

895 6 Conclusions

896

897 We processed and analyzed high-rate (30-s) GPS solutions recorded during the first month after
 898 the M_w 9.0 Tohoku-Oki megathrust earthquake (2011), and complemented this dataset with daily
 899 solutions at larger timescales, up to ~9 years after the mainshock. This allowed us to explore the
 900 kinematics of postseismic deformation following a megathrust earthquake over an unprecedented
 901 range of timescales, hence to constrain the nature of the underlying physical processes. We found
 902 that early postseismic time series (minutes to months) can be explained by an afterslip
 903 mechanism with a $p < 1$ “Omori-like” signature for the velocities, in disagreement with the
 904 prediction of a rate-and-state velocity-strengthening rheology for a frictional interface (which

905 would imply a $p \approx 1$). We argue instead that this early postseismic deformation results from a
906 transient brittle creep mechanism within an unruptured section of the fault and its surroundings,
907 corresponding to the cumulative effect of stress- and thermally activated local slip/deformation
908 events. The regional variations of the p -value indicate that the area affected by the the Ibaraki-
909 Oki aftershock is associated to a $p \sim 1$, that could be due to a negative thermal anomaly in this
910 region.

911 At larger timescales (years), this transient afterslip mechanism underestimates the surface
912 seaward motions observed by the land GPS stations. Afterslip can explain neither the landward
913 motions observed by a few offshore GPS stations nor the exponential decay of the inland GPS
914 velocities, that are likely a signature of viscoelastic mantellic deformation, which becomes
915 significant at multiyear timescales.

916
917 In the future, it would be of upmost interest to extend such analysis to other megathrust
918 earthquakes. This would allow to determine whether the characteristics of the Tohoku-Oki
919 postseismic deformation are common or rather an exception.
920

921 **Acknowledgments, Samples, and Data**

922

923 This work has benefited from fruitful discussions with Hugo Perfettini.

924 This study has been supported by the Agence Nationale de la Recherche (ANR-17-CE31-0002-
925 01) AtypicSSE project. The authors are very grateful to the Geospatial Information Authority of
926 Japan (GSI) for making the GEONET GNSS data available. MR acknowledges the support of the
927 Face foundation (Thomas Jefferson Fund TJF19-21).

928 The GNSS data processing presented in this paper was performed using the GRICAD
929 infrastructure (<https://gricad.univ-grenoble-alpes.fr>), which is supported by Grenoble research
930 communities.

931

932 Raw daily GNSS time series data are accessible on the Observatoire des Sciences de l'Univers de
933 Grenoble website associated to the DOI: <https://doi.org/10.17178/GNSS.products.Japan>.

934 Kinematic GNSS time series are accessible on .. (in progress)

935 Static GNSS time series are accessible on .. (in progress)

936

937

938

939

940

941

942

943

944 **References**

- 945
946 Altamimi, Z., Rebischung, P., Métivier, L., & Collilieux, X. (2016). ITRF2014 : A new release
947 of the International Terrestrial Reference Frame modeling nonlinear station motions: ITRF2014.
948 *Journal of Geophysical Research: Solid Earth*, 121(8), 6109-6131.
949 <https://doi.org/10.1002/2016JB013098>
- 950 Amitrano, D. (2003). Brittle-ductile transition and associated seismicity : Experimental and
951 numerical studies and relationship with the b value: BRITTLE-DUCTILE TRANSITION AND
952 SEISMICITY. *Journal of Geophysical Research: Solid Earth*, 108(B1).
953 <https://doi.org/10.1029/2001JB000680>
- 954 Amitrano, D., Grasso, J.-R., & Hantz, D. (1999). From diffuse to localised damage through
955 elastic interaction. *Geophysical Research Letters*, 26(14), 2109-2112.
956 <https://doi.org/10.1029/1999GL900388>
- 957 Amitrano, D., & Helmstetter, A. (2006). Brittle creep, damage, and time to failure in rocks :
958 TIME TO FAILURE IN ROCKS. *Journal of Geophysical Research: Solid Earth*, 111(B11), n/a-
959 n/a. <https://doi.org/10.1029/2005JB004252>
- 960 Andrade, E. N. D. C. (1910). On the viscous flow in metals, and allied phenomena. *Proceedings*
961 *of the Royal Society of London. Series A, Containing Papers of a Mathematical and Physical*
962 *Character*, 84(567), 1-12. <https://doi.org/10.1098/rspa.1910.0050>
- 963 Baumberger, T., Berthoud, P., & Caroli, C. (1999). Physical analysis of the state- and rate-
964 dependent friction law. II. Dynamic friction. *Physical Review B*, 60(6), 3928-3939.
965 <https://doi.org/10.1103/PhysRevB.60.3928>
- 966 Bertiger, W., Desai, S. D., Haines, B., Harvey, N., Moore, A. W., Owen, S., & Weiss, J. P.
967 (2010). Single receiver phase ambiguity resolution with GPS data. *Journal of Geodesy*, 84(5),
968 327-337. <https://doi.org/10.1007/s00190-010-0371-9>
- 969 Bilitza, D., Altadill, D., Zhang, Y., Mertens, C., Truhlik, V., Richards, P., McKinnell, L.-A., &
970 Reinisch, B. (2014). The International Reference Ionosphere 2012 – a model of international
971 collaboration. *Journal of Space Weather and Space Climate*, 4, A07.
972 <https://doi.org/10.1051/swsc/2014004>
- 973 Boehm, J., Niell, A., Tregoning, P., & Schuh, H. (2006). Global Mapping Function (GMF) : A
974 new empirical mapping function based on numerical weather model data. *Geophysical Research*

- 975 Letters, 33(7), L07304. <https://doi.org/10.1029/2005GL025546>
- 976 Bortz, A. B., Kalos, M. H., & Lebowitz, J. L. (1975). A New Algorithm for Monte Carlo
977 Simulation of king Spin Systems. *Journal of Computational Physics*, 17, 9.
- 978
- 979 Carter, N. L., & Kirby, S. H. (1978). Transient creep and semibrittle behavior of crystalline
980 rocks. 33.
- 981 Castellanos, D. F., & Zaiser, M. (2018). Avalanche Behavior in Creep Failure of Disordered
982 Materials. *Physical Review Letters*, 121(12), 125501.
983 <https://doi.org/10.1103/PhysRevLett.121.125501>
- 984 Choi, K. (2007). Improvements in GPS Precision : 10 Hz to One Day. 255.
- 985 Cottrell, A. H. (1952). The time laws of creep. *Journal of the Mechanics and Physics of Solids*,
986 1(1), 53-63. [https://doi.org/10.1016/0022-5096\(52\)90006-9](https://doi.org/10.1016/0022-5096(52)90006-9)
- 987 Dieterich, J. H. (1979). Modeling of rock friction : 1. Experimental results and constitutive
988 equations. *Journal of Geophysical Research*, 84(B5), 2161.
989 <https://doi.org/10.1029/JB084iB05p02161>
- 990 Fukuda, J., Johnson, K. M., Larson, K. M., & Miyazaki, S. (2009). Fault friction parameters
991 inferred from the early stages of afterslip following the 2003 Tokachi-oki earthquake. *Journal of*
992 *Geophysical Research*, 114(B4). <https://doi.org/10.1029/2008JB006166>
- 993 Fukuda, J., Kato, A., Kato, N., & Aoki, Y. (2013). Are the frictional properties of creeping faults
994 persistent? Evidence from rapid afterslip following the 2011 Tohoku-oki earthquake:
995 AFTERSLIP AND FAULT FRICTION PROPERTIES. *Geophysical Research Letters*, 40(14),
996 3613-3617. <https://doi.org/10.1002/grl.50713>
- 997 Girard, L., Amitrano, D., & Weiss, J. (2010). Failure as a critical phenomenon in a progressive
998 damage model. *Journal of Statistical Mechanics: Theory and Experiment*, 2010(01), P01013.
999 <https://doi.org/10.1088/1742-5468/2010/01/P01013>
- 1000 Griggs, D. (1939). Creep of Rocks.
- 1001 Hayes, G. P., Moore, G. L., Portner, D. E., Hearne, M., Flamme, H., Furtney, M., & Smoczyk,
1002 G. M. (2018). Slab2, a comprehensive subduction zone geometry model. *Science*, 362(6410),
1003 58-61. <https://doi.org/10.1126/science.aat4723>
- 1004 Helmstetter, A., & Shaw, B. E. (2009). Afterslip and aftershocks in the rate-and-state friction

1005 law : AFTERSHOCKS AND RATE-AND-STATE FRICTION. *Journal of Geophysical*
 1006 *Research: Solid Earth*, 114(B1). <https://doi.org/10.1029/2007JB005077>

1007 Heslot, F., Baumberger, T., Perrin, B., Caroli, B., & Caroli, C. (1994). Creep, stick-slip, and dry-
 1008 friction dynamics : Experiments and a heuristic model. *Physical Review E*, 49(6), 4973-4988.
 1009 <https://doi.org/10.1103/PhysRevE.49.4973>

1010 Hsu, Y.-J. (2006). Frictional Afterslip Following the 2005 Nias-Simeulue Earthquake, Sumatra.
 1011 *Science*, 312(5782), 1921-1926. <https://doi.org/10.1126/science.1126960>

1012 Hu, Y., Bürgmann, R., Freymueller, J. T., Banerjee, P., & Wang, K. (2014). Contributions of
 1013 poroelastic rebound and a weak volcanic arc to the postseismic deformation of the 2011 Tohoku
 1014 earthquake. *Earth, Planets and Space*, 66(1), 106. <https://doi.org/10.1186/1880-5981-66-106>

1015 Ingleby, T., & Wright, T. J. (2017). Omori-like decay of postseismic velocities following
 1016 continental earthquakes : OMORI DECAY OF POSTSEISMIC VELOCITIES. *Geophysical*
 1017 *Research Letters*, 44(7), 3119-3130. <https://doi.org/10.1002/2017GL072865>

1018 Ji, Y., Yoshioka, S., Manea, V. C., Manea, M., & Matsumoto, T. (2016). Three-dimensional
 1019 numerical modeling of thermal regime and slab dehydration beneath Kanto and Tohoku, Japan.
 1020 *Journal of Geophysical Research*, 22.

1021 Langbein, J. (2006). Coseismic and initial postseismic deformation from the 2004 Parkfield,
 1022 California earthquake, observed by GPS, EDM, creepmeters, and borehole strainmeters. 56.

1023 Lay, T. (2018). A review of the rupture characteristics of the 2011 Tohoku-oki Mw 9.1
 1024 earthquake. *Tectonophysics*, 733, 4-36. <https://doi.org/10.1016/j.tecto.2017.09.022>

1025 Malservisi, R., Schwartz, S. Y., Voss, N., Protti, M., Gonzalez, V., Dixon, T. H., Jiang, Y.,
 1026 Newman, A. V., Richardson, J., Walter, J. I., & Voyerko, D. (2015). Multiscale postseismic
 1027 behavior on a megathrust : The 2012 Nicoya earthquake, Costa Rica: POSTSEISMIC 2012
 1028 NICOYA EARTHQUAKE. *Geochemistry, Geophysics, Geosystems*, 16(6), 1848-1864.
 1029 <https://doi.org/10.1002/2015GC005794>

1030 Marill, L., Marsan, D., Socquet, A., Radiguet, M., Cotte, N., & Rousset, B. (2021). 14-year
 1031 acceleration along the Japan Trench. *Journal of Geophysical Research: Solid Earth*.
 1032 <https://doi.org/10.1029/2020JB021226>

1033 Marone, C. (1998). Laboratory-Derived Friction Laws and Their Application to Seismic
 1034 Faulting. *Annual Review of Earth and Planetary Sciences*, 26(1), 643-696.
 1035 <https://doi.org/10.1146/annurev.earth.26.1.643>

- 1036 Marone, C. J., Scholtz, C. H., & Bilham, R. (1991). On the mechanics of earthquake afterslip.
1037 *Journal of Geophysical Research*, 96(B5), 8441. <https://doi.org/10.1029/91JB00275>
- 1038 Marquez-Azua, B., & DeMets, C. (2003). Crustal velocity field of Mexico from continuous GPS
1039 measurements, 1993 to June 2001 : Implications for the neotectonics of Mexico. 20.
- 1040 Miyazaki, S., & Larson, K. M. (2008). Coseismic and early postseismic slip for the 2003
1041 Tokachi-oki earthquake sequence inferred from GPS data. *Geophysical Research Letters*, 35(4).
1042 <https://doi.org/10.1029/2007GL032309>
- 1043 Montési, L. G. J. (2004). Controls of shear zone rheology and tectonic loading on postseismic
1044 creep : TIME DEPENDENCE OF POSTSEISMIC CREEP. *Journal of Geophysical Research:*
1045 *Solid Earth*, 109(B10). <https://doi.org/10.1029/2003JB002925>
- 1046 Morikami, S., & Mitsui, Y. (2020). Omori-like slow decay ($p < 1$) of postseismic displacement
1047 rates following the 2011 Tohoku megathrust earthquake. *Earth, Planets and Space*, 72(1), 37.
1048 <https://doi.org/10.1186/s40623-020-01162-w>
- 1049 Munekane, H. (2012). Coseismic and early postseismic slips associated with the 2011 off the
1050 Pacific coast of Tohoku Earthquake sequence : EOF analysis of GPS kinematic time series.
1051 *Earth, Planets and Space*, 64(12), 1077-1091. <https://doi.org/10.5047/eps.2012.07.009>
- 1052 Nishimura, T., Munekane, H., & Yurai, H. (2011). The 2011 off the Pacific coast of Tohoku
1053 Earthquake and its aftershocks observed by GEONET. *Earth, Planets and Space*, 63(7), 631-363.
1054 <https://doi.org/10.5047/eps.2011.06.025>
- 1055 Okada, Y. (1992). Internal deformation due to shear and tensile faults in a half-space. *Bulletin of*
1056 *the Seismological Society of America*, 82(2), 1018-1040.
- 1057 Ozawa, S., Nishimura, T., Munekane, H., Suito, H., Kobayashi, T., Tobita, M., & Imakiire, T.
1058 (2012). Preceding, coseismic, and postseismic slips of the 2011 Tohoku earthquake, Japan :
1059 AFTERSLIP OF THE TOHOKU EARTHQUAKE. *Journal of Geophysical Research: Solid*
1060 *Earth*, 117(B7), n/a-n/a. <https://doi.org/10.1029/2011JB009120>
- 1061 Perfettini, H., & Ampuero, J.-P. (2008). Dynamics of a velocity strengthening fault region :
1062 Implications for slow earthquakes and postseismic slip. *Journal of Geophysical Research*,
1063 113(B9). <https://doi.org/10.1029/2007JB005398>
- 1064 Perfettini, H., & Avouac, J. P. (2014). The seismic cycle in the area of the 2011 M w 9.0
1065 Tohoku-Oki earthquake. *Journal of Geophysical Research: Solid Earth*, 119(5), 4469-4515.
1066 <https://doi.org/10.1002/2013JB010697>

- 1067 Perfettini, H., & Avouac, J.-P. (2004). Postseismic relaxation driven by brittle creep : A possible
 1068 mechanism to reconcile geodetic measurements and the decay rate of aftershocks, application to
 1069 the Chi-Chi earthquake, Taiwan: DYNAMICS OF BRITTLE CREEP. *Journal of Geophysical*
 1070 *Research: Solid Earth*, 109(B2). <https://doi.org/10.1029/2003JB002488>
- 1071 Perfettini, H., Avouac, J.-P., Tavera, H., Kositsky, A., Nocquet, J.-M., Bondoux, F., Chlieh, M.,
 1072 Sladen, A., Audin, L., Farber, D. L., & Soler, P. (2010). Seismic and aseismic slip on the Central
 1073 Peru megathrust. *Nature*, 465(7294), 78-81. <https://doi.org/10.1038/nature09062>
- 1074 Radiguet, M., Cotton, F., Vergnolle, M., Campillo, M., Valette, B., Kostoglodov, V., & Cotte, N.
 1075 (2011). Spatial and temporal evolution of a long term slow slip event : The 2006 Guerrero Slow
 1076 Slip Event: Evolution of the 2006 Guerrero SSE. *Geophysical Journal International*, 184(2),
 1077 816-828. <https://doi.org/10.1111/j.1365-246X.2010.04866.x>
- 1078 Radiguet, M., Perfettini, H., Cotte, N., Gualandi, A., Valette, B., Kostoglodov, V., Lhomme, T.,
 1079 Walpersdorf, A., Cabral Cano, E., & Campillo, M. (2016). Triggering of the 2014 M w 7.3
 1080 Papanoa earthquake by a slow slip event in Guerrero, Mexico. *Nature Geoscience*, 9(11),
 1081 829-833. <https://doi.org/10.1038/ngeo2817>
- 1082 Rice, J. R., & Tse, S. T. (1986). Dynamic motion of a single degree of freedom system following
 1083 a rate and state dependent friction law. 10.
- 1084 Savage, J. C. (2007). Postseismic relaxation associated with transient creep rheology. *Journal of*
 1085 *Geophysical Research*, 112(B5), B05412. <https://doi.org/10.1029/2006JB004688>
- 1086 Savage, J. C., Svarc, J. L., & Yu, S.-B. (2005). Postseismic relaxation and transient creep :
 1087 POSTSEISMIC RELAXATION AND CREEP. *Journal of Geophysical Research: Solid Earth*,
 1088 110(B11). <https://doi.org/10.1029/2005JB003687>
- 1089 Scholz, C. H. (1968). Mechanism of creep in brittle rock. *Journal of Geophysical Research*,
 1090 73(10), 3295-3302. <https://doi.org/10.1029/JB073i010p03295>
- 1091 Selle, C., & Desai, S. (2016). Optimization of tropospheric delay estimation parameters by
 1092 comparison of GPS-based precipitable water vapor estimates with microwave radiometer
 1093 measurements. 17.
- 1094 Sobrero, F. S., Bevis, M., Gómez, D. D., & Wang, F. (2020). Logarithmic and exponential
 1095 transients in GNSS trajectory models as indicators of dominant processes in postseismic
 1096 deformation. *Journal of Geodesy*, 94(9), 84. <https://doi.org/10.1007/s00190-020-01413-4>
- 1097 Spiridonov, E. A., & Vinogradova, O. Yu. (2020). Oceanic Tide Model FES2014b : Comparison

1098 with Gravity Measurements. *Izvestiya, Atmospheric and Oceanic Physics*, 56(11), 1432-1446.
1099 <https://doi.org/10.1134/S0001433820110092>

1100 Sun, T., & Wang, K. (2015). Viscoelastic relaxation following subduction earthquakes and its
1101 effects on afterslip determination. *Journal of Geophysical Research: Solid Earth*, 120(2),
1102 1329-1344. <https://doi.org/10.1002/2014JB011707>

1103 Sun, T., Wang, K., Iinuma, T., Hino, R., He, J., Fujimoto, H., Kido, M., Osada, Y., Miura, S.,
1104 Ohta, Y., & Hu, Y. (2014). Prevalence of viscoelastic relaxation after the 2011 Tohoku-oki
1105 earthquake. *Nature*, 514. <https://doi.org/10.1038/nature13778>

1106 Tajima, F., Mori, J., & Kennett, B. L. N. (2013). A review of the 2011 Tohoku-Oki earthquake
1107 (Mw 9.0) : Large-scale rupture across heterogeneous plate coupling. *Tectonophysics*, 586, 15-34.
1108 <https://doi.org/10.1016/j.tecto.2012.09.014>

1109 Tobita, M. (2016). Combined logarithmic and exponential function model for fitting postseismic
1110 GNSS time series after 2011 Tohoku-Oki earthquake. *Earth, Planets and Space*, 68(1), 41.
1111 <https://doi.org/10.1186/s40623-016-0422-4>

1112 Tsang, L. L. H., Vergnolle, M., Twardzik, C., Sladen, A., Nocquet, J.-M., Rolandone, F.,
1113 Agurto-Detzel, H., Cavalié, O., Jarrin, P., & Mothes, P. (2019). Imaging rapid early afterslip of
1114 the 2016 Pedernales earthquake, Ecuador. *Earth and Planetary Science Letters*, 524, 115724.
1115 <https://doi.org/10.1016/j.epsl.2019.115724>

1116 Twardzik, C., Vergnolle, M., Sladen, A., & Avallone, A. (2019). Unravelling the contribution of
1117 early postseismic deformation using sub-daily GNSS positioning. *Scientific Reports*, 9(1).
1118 <https://doi.org/10.1038/s41598-019-39038-z>

1119 Wang, K., Hu, Y., & He, J. (2012). Deformation cycles of subduction earthquakes in a
1120 viscoelastic Earth. *Nature*, 484(7394), 327-332. <https://doi.org/10.1038/nature11032>

1121 Wang, K., Sun, T., Brown, L., Hino, R., Tomita, F., Kido, M., Iinuma, T., Kodaira, S., &
1122 Fujiwara, T. (2018). Learning from crustal deformation associated with the M9 2011 Tohoku-oki
1123 earthquake. *Geosphere*, 14(2), 552-571. <https://doi.org/10.1130/GES01531.1>

1124 Zumberge, J. F., Heflin, M. B., Jefferson, D. C., Watkins, M. M., & Webb, F. H. (1997). Precise
1125 point positioning for the efficient and robust analysis of GPS data from large networks. *Journal*
1126 *of Geophysical Research: Solid Earth*, 102(B3), 5005-5017. <https://doi.org/10.1029/96JB03860>

1127
1128